# Theoretical and Experimental Study of Solid Oxide Fuel Cell (SOFC) Using Impedance Spectra

by

Yeqing Fu

B.S., Tsinghua University (2006)
M.S., Tsinghua University (2008)
M.S.CEP, Massachusetts Institute of Technology (2013)

Submitted to the Department of Chemical Engineering
in partial fulfillment of the requirement for the degree of

Doctor of Philosophy in Chemical Engineering

at the

MASSACHUSETTS INSTITUTE OF TECHNOOGY

June 2014



Author.....
Department of Chemical Engineering
June23rd, 2014

Certified by.....
Martin Z. Bazant
Professor of Chemical Engineering and Mathematics
Thesis Supervisor

Accepted by.....
Patrick S. Doyle
Singapore Research Professor of Chemical Engineering
Chairman, Committee for Graduate Students

# Theoretical and Experimental Study of Solid Oxide Fuel Cell (SOFC) Using Impedance Spectra

by

Yeqing Fu

Submitted to the Department of Chemical Engineering
on June25, 2014, in partial fulfillment of the requirement for the degree of
Doctor of Philosophy in Chemical Engineering

**ABSTRACT**

Solid oxide fuel cell (SOFC) is a promising alternative energy source, with its advantages of high operating efficiency, fuel flexibility, low emissions and relatively low cost. However, there are several challenges concerning the SOFC research. Little is known about the complex interfacial electrochemistry and thermochemistry, and it is also difficult to diagnose problems and optimize cell performance. Therefore, physics-based models are needed to better understand the underlying mechanisms of SOFCs.

This research work addressed two important aspects of the numerical modeling of SOFCs: the multicomponent gas diffusion in porous electrode at the anode and the heterogeneous electrocatalysis of oxygen reduction reaction (ORR) at the cathode.

First, anode was diagnosed to be mainly controlled by multicomponent gas diffusion inside the anode bulk (supporting) layer, and the Dusty Gas model is identified as an appropriate model to describe the gas diffusion resistance extracted from no bias AC impedance. Anode-supported SOFCs with Ni-yttria-stabilized zirconia (YSZ) anode were used to study the multicomponent gas transport in porous electrodes. A fuel gas mixture of $H_2$-$H_2O$-$N_2$ was fed to the anode and AC impedance data were measured at 800ºC by varying hydrogen partial pressure at both no bias and a current of 300 mA. Impedance data were also collected at no bias at three different temperatures (800ºC, 850ºC and 900ºC). For the first time, three models were used to analytically derive the diffusion resistance ($R_b$), which was then compared to the values extracted from experimental impedance data. The Dusty Gas model yields the best predictions and the tortuosity

values derived from Dusty Gas model are found to be independent of feeding gas composition, operating current and temperatures, which is consistent with the fundamental or underlying physics. Moreover, with the anode porosity known to be approximately 46%, the tortuosity derived from the Dusty Gas model is 2.3~3.3, which matches both theoretical expectations and experimental measurements. This gas diffusion resistance analysis using AC impedance greatly improves the way to study the multicomponent gas diffusion within porous electrodes.

Secondly, electrocatalysis at the SOFC cathode was studied using symmetric cathode cells, whose no bias AC impedance was investigated and modeled using a physics-based electrocatalysis model, describing the coupled dissociative adsorption of oxygen molecules onto the catalytic lanthanum strontium manganite (LSM) particles and surface diffusion of adsorbed species, assuming the charge transfer reaction is relatively fast and at equilibrium. A Gerischer type impedance response with a reflecting boundary condition was theoretically derived assuming the oxygen adsorption follows Langmuir type kinetics. This cathode electrocatalysis model not only captures the frequency dependence of the no bias AC impedance, it also well represents the oxygen partial pressure ($pO_2$) dependence. Four different impedance curves at $pO_2$ of 21%, 15%, 10% and 5% were fitted at the same time, and the model was able to well describe them using one set of physically meaningful fitting parameters. Microstructure of the cathode functional layer (CFL) was also studied using this electrocatalysis model. It was found that the diffusion length $L_s$ is a critical parameter, whose ratio with respect to the characteristic boundary layer length $l_\delta$ (the Thiele modulus) critically controls the effectiveness of the catalytic activity of the cathode functional layer.

These understandings of the anode gas diffusion and cathode electrocatalytic process was used to propose an equivalent circuit for the full solid oxide fuel cell, which captures all important resistances in the SOFC, but is still as simple as possible, in order to minimize the number of fitting parameters. This full cell model greatly helps to break down the AC impedance which has overlapped responses from several processes. The analysis identified the rate limiting step of the full Saint-Gobain button cell to be the cathode electrocatalytic process, which indicates that in order to improve the cell performance,

research should be focused on improving the cathode functional layer, by either improving the surface catalytic activity of the LSM particles, or changing the microstructure of the cathode functional layer.

.

Thesis Supervisor: Martin Z. Bazant

Title: Professor of Chemical Engineering and Mathematics.

*To my husband Zan, my daughter Kelly, my son Kevin and my parents Jishu and Yajun.*

# Acknowledgements

In retrospect on the years I have spent at MIT, I am full of gratitude and thanks to many people. First and foremost, I would like to express my deepest appreciation to my thesis advisor Prof. Martin Z. Bazant whose intelligence, diligence, enthusiasm and philosophy have had a big impact on me, not only in my research but also in my daily life. Prof. Bazant's great passion on tackling real-world challenges by incorporating fundamental theories and scientific rules into engineering research work has inspired me a lot. I thank Prof. Bazant for his consistent trust and support during my thesis work. Whenever I got stuck with my research, he was always available to provide kind help with lots of encouragement and inspiration. This gave me a lot of strength and motivated me going through some of the difficult days of my PhD life. Prof. Bazant also made me realize and believe that most questions can be answered in a 'simpler' way by a careful theoretical argument, without carrying out a full numerical simulation. Sometimes an insightful analysis with a deep understanding is much more effective, efficient, and full of beauty.

I am also honored to have Prof. William M. Deen and Prof. Yang Shao-Horn on my thesis committee. Their diverse expertise and perspectives have greatly enriched my educational and research experience. Professor Deen provided me with very helpful insights on mass transport in porous media and valuable suggestions on the importance of model comparisons. His encouragement for me in understanding the history of Dusty Gas model, Knudsen diffusivity is much appreciated. Prof. Shao-Horn was essential in helping me to better understand the research and history in electrochemistry, and especially in the area of solid oxide fuel cell. She has solid and profound knowledge about the cutting edge research in SOFC community, and in general electrochemistry as well, and have given me lots of useful suggestions on how to set up a reasonable model for Saint-Gobain cell, and which electrode would potentially be the rate limiting factor.

I would also like to extend my appreciation to Dr. Yi Jiang, the former liaison of the Saint-Gobain SOFC project. All the important experiments in my thesis were executed in his electrochemistry testing lab with the help of his team members. His support and

generosity to allow me to design experiments and collect data in his testing lab is greatly appreciated. Discussions with Dr. Yi Jiang also greatly inspired me to become an engineer in industry, aiming to tackle with real world engineering challenges. His beautiful way of leading a team and smoothly communicating with upper and lower levels also encourages me a lot in improving my communication skills and professionalism. Dr. Aravind Mohanram is another person that I owe my gratitude to. He led the latter part of this project, and has made tremendous efforts in connecting the research of MIT and Saint-Gobain. Under his influence, the cathode model was well developed, and then used to connect the microstructure-performance relationship. His insightful comments and suggestions during each update meeting has inspired and guided us through a difficult and dark period, and has made the model useful in determining the rate limiting step of the Saint-Gobain full cell.

I would also like to acknowledge some other important people at Saint-Gobain. Dr. Abhijit Dutta gave me a lot of detailed instructions on modeling Saint-Gobain's SOFC system, and also provided generous support and help in preparing for the scientific papers. Detailed discussion with him has helped me save lots of research time in building numerical models. Dr. Li Sun and Dr. Frank Qi also gave me a lot of suggestions and comments on how to analyze complicated impedance data, and how to compare responses of button cells with those of the stack cells. I really enjoyed and valued the brainstorms I had with them.

I would also give special thanks to Dr. Sophie Poizeau, who tried to transform the scientific results of my work into engineering implications and deliverables for Saint-Gobain's SOFC team. Her enthusiasm and great efforts exerted in this aspect is greatly appreciated.

I also need to thank those who gave me rides to and from the Saint-Gobain Northboro research center, including Jane Chen-Liang, Robin Barabasz, Dr. Abhijit Dutta and Dr. Sophie Poizeau. All the update meetings held at the Northboro research center won't happen without their kind help.

I would like to acknowledge my collaborators and friends, especially Dr. Antonio Bertei, a visitor from University of Pisa, Italy. His intelligence and diligent work in

incorporating my cathode surface model into his full numerical simulation scheme has deepened my understanding of the model in a more broadened way. Bazant group members, especially Dr Todd R. Ferguson, also provided me with lots of help in coding and debugging in the early stage of the project.

I would like to thank my friends too, especially Xiangdong Liang, Lifang Zhou, and Xiaoxiang Zhu. The friendship I developed here is an unforgettable memory. They gave me great support and encouragement for my research and life here. They also offered their generosity in my job hunting.

Finally, I would like to add a special thanks to my dear family members. It has been 6 years since I left China to pursue my PhD degree at MIT. It is their selfless support and understanding that made me go through my PhD life, which is full of ups and downs. I would like to thank my husband Zan, whose support and love over the years have made my life here much enjoyable and colorful. We had our daughter Kelly and our son Kevin during my PhD life. These little angels also brought me joys, responsibilities and motivations. My mother Yajun and mother-in-law Fenglun provided tremendous helps in taking care of the babies. They had to travel overseas to offer their help for as long as six month each time. Both of them have spent more than 1.5 years in total at MIT, being far away from their own husbands and other family members. I definitely owe a lot to them. Special thanks to both of them too.

# Contents

# List of Figures

# List of Tables

# Chapter 1. Introduction

## 1.1 Fuel cells

A fuel cell is an energy conversion device that converts the chemical energy of a fuel directly to electrical energy and heat, without the need for direct combustion as an intermediate step. It gives much higher conversion efficiencies than conventional thermo-mechanical methods. Similar to batteries, the operating principles of fuel cells are electrochemical combination of reactants to generate electricity. In fuel cell a combination of a gaseous fuel (e.g. hydrogen or hydrocarbon fuels) and an oxidant gas (e.g. oxygen in the air) go through electrodes and half-cell reaction occurs on anode and cathode respectively, with the active charge carrier species going through an ion conducting electrolyte. In this way, electrons are released into external circuit to produce electricity. However, unlike a battery, a fuel cell does not require recharging. A fuel cell operates as long as both fuel and oxidant are supplied to the electrodes and is environment friendly, with negligible influence exerted on the natural environment.

Fuel cells are generally classified by the chemical characteristics of the electrolyte used as the ionic conductor in the cell. By far the greatest research interest throughout the world has focused on Proton Exchange Membrane fuel cells (PEMFCs) and Solid Oxide fuel cells (SOFCs).

## 1.2 Solid oxide fuel cells

SOFC is a high temperature fuel cell technology. They are extremely useful in large, high-power applications such as full-scale industrial stations and large-scale electricity-generating stations. SOFC system usually utilizes a solid ceramic as the electrolyte and operates at extremely high temperatures (600°C~1000°C). This high operating temperature allows internal reforming, promotes rapid electro-catalytic reactions with

non-precious metals, and produces high quality byproduct heat for co-generation. Efficiencies for this type of fuel cell can reach up to 70%.

SOFC technology is very demanding from a materials standpoint and has potential advantages and competitiveness in the following aspects. 1) It is the most efficient fuel cell in terms of generating electricity. Moreover, the high operating temperature of SOFCs produces high quality heat byproduct which can be used for co-generation or combined cycle applications. This can further increase the overall energy efficiency. 2) It is flexible in the choice of fuels such as hydrocarbon fuels, e.g., natural gas. 3) SOFCs do not need expensive noble metals that could be issues in resource availability and cost. 4) Any carbon monoxide produced is converted to carbon dioxide at the high operating temperature; therefore SOFCs have very low emissions in exhaust gases.

SOFCs are composed of all-solid-state materials. And the solid state character of all SOFC components puts no fundamental restriction on the cell configuration. Cells are being constructed in many different configurations, such as planar button cell, flat-plates cells, tubular cells or rolled tubes.

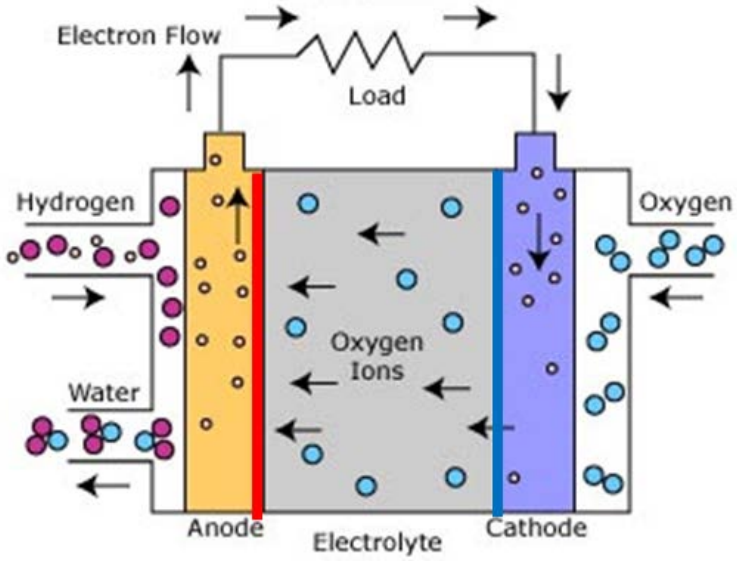


**Figure 1-1 Demonstration of the SOFC, when hydrogen carried by nitrogen and 3% water mixture is used as fuel at the anode side and oxygen carried by air is fed from the cathode side[1]. (Not drawn to scale)**

A SOFC consists of two electrodes sandwiched around a hard ceramic electrolyte such as the remarkable ceramic material called zirconia (Figure 1-1). Fuel gas such as hydrogen is fed into the anode of the fuel cell and oxygen, usually carried by air, enters the cell via the cathode. The anode disperses the hydrogen gas equally over its whole surface and conducts the electrons that are freed from hydrogen molecule, to be used as power in the external circuit. The cathode distributes the oxygen fed to it onto its surface and conducts the electrons back from the external circuit where they can recombine with oxygen ions, passed across the electrolyte, and hydrogen to form water. The electrolyte determines the operating temperature of the fuel cell and is used to prevent the two electrodes to come into electronic contact by blocking the electrons. It also allows the flow of charged ions from one electrode to the other to maintain the overall charge balance.

Each component of the SOFC serves several functions and must therefore meet certain requirements such as proper stability (chemical, phase, morphological, and dimensional), proper conductivity, chemical compatibility with other components, similar thermal expansion to avoid cracking during the cell operation, dense electrolyte to prevent gas mixing, porous anode and cathode to allow gas transport to the reaction sites, high strength and toughness properties, easiness to be fabricated, amenable to particular fabrication conditions, compatibility at higher temperatures at which the ceramic structures are fabricated, relatively low cost, etc.

## 1.3 Voltage losses (polarization) in SOFCs

When the fuel cell is connected to a load through a closed circuit, a current is produced through the electrochemical reactions and the cell's potential is reduced by internal non-reversible voltage losses which depend on the current and derive from the following three mechanisms.

• Ohmic resistance losses: which occur in the solid electrolyte phases due to ions flow and in the electrode phases and metallic interconnects due to electrons flow. It is caused by the electrical resistances of the electrodes and resistance of ion transport in the electrolyte. The area-specific resistance (ASR) is based on $1cm^2$ of the cell. Three general

methods of reducing this polarization are the use of high conductivity electrodes, the use of appropriate interconnect materials and design, and the use of thin electrolyte.

• Concentration overpotentials: reduced Nernst potential at the electrochemically active reaction zone (triple phase boundary, TPB) due to depletion of charge carrying reactants caused by slow diffusion from the bulk of the gas chambers/channels through the porous electrodes.

• Activation overpotentials: reduced electrochemical potential because energy is needed to drive the electrochemical reactions in the desired forward direction, i.e. reduction of oxygen at the cathode and oxidation of fuel gases (e.g.,hydrogen) at the anode.

The operating cell potential thus can be calculated as a subtraction of the above different losses from the reversible potential.

## 1.4 Electrochemical impedance spectroscopy (EIS)

AC impedance is a more general type of resistance. Its modulus and phase are dependent on the frequency. In measurements, if we use a sinusoidal voltage signal, $v(t) = V\cos(2\pi ft + \phi)$, to excite a linear time-invariant circuit system, then we can get an AC current response, $i(t) = I\cos(2\pi ft + \psi)$, which has the same frequency as v(t). V and $\phi$ denote the amplitude and the initial phase of v(t), respectively. In the same way, I and $\psi$ denote the amplitude and the initial phase of i(t), respectively. Normally, the expressions of voltage and current can be mapped and converted from a time domain to a complex domain: $v^*(t) = V\exp(2\pi ft + \phi)$ and $i^*(t) = I\exp(2\pi ft + \psi)$, respectively, where $v(t) = \mathrm{Re}[v^*(t)]$, and $i(t) = \mathrm{Re}[i^*(t)]$. Therefore, there exists a simple one-to-one correspondence between the time domain and frequency domain expressions.

AC impedance, $Z(j\omega)$, can be expressed as $Z(j\omega) = Z_{Re} + j^*Z_{Im}$, where $Z_{Re}$ is the real part and $Z_{Im}$ is the imaginary part[2], and j is the square root of -1. The plot of $Z_{Im}$ versus $Z_{Re}$ is called a Nyquist plot. It is worth noting that the Nyquist plot does not show the corresponding frequency for any data point on the plot. Another popular presentation method for $Z(j\omega)$ is the Bode plot. The impedance is plotted with the log frequency on the x-axis and both the log absolute value of the impedance $|Z(j\omega)|$ and the phase-shift

on the y-axis. Unlike the Nyquist plot, the Bode plot explicitly shows frequency information. Often, Nyquist and Bode plots are presented together to give a clearer picture of the AC impedance. Three-dimensional perspective plotting is another alternative method for impedance display[3]. The shapes of the impedance plots reflect the variation of many factors and parameters in SOFCs, and based on this, useful information about the material, composition, microstructure, and operation conditions can be obtained.

In contrast to IV curves, where only the overall loss of a cell can be identified, the electrical impedance spectroscopy (EIS) is one of the most promising methods for unfolding complex electrochemical systems, and has proven to be a powerful tool in investigating different polarization processes in a solid oxide fuel cell (SOFC). It takes the advantage from the fact that the polarization loss mechanisms taking place in an electrochemical system differ in their characteristic time constant and frequency response, and therefore it is used for characterizing materials, elucidating electrochemical mechanisms, assessing transport properties, and characterizing cell, stack, and system performance[4,5]. The most typical and standard approach to measure the dynamic behavior is by applying a sinusoidal AC current or voltage on top of a DC bias for a range of frequencies in order to generate the EIS.

Experimental impedance data are usually interpreted using an appropriate model of the electrochemical system, and parameters are obtained by fitting simulated impedance spectra to experimental data. Depending on the model, the parameters can be attributed a physical or chemical meaning, or remain a purely empirical description of the system.

In theory, each process, including transport and electrochemical reaction, should have its own arc in the electrochemical impedance spectrum. However, due to their capacitive nature, the processes need a certain time to relax when perturbed by a changing boundary condition, and therefore their responses tend to have overlapped arcs in the EIS curves. In practice, the electrochemical impedance spectrum is a superimposition of arcs of different sizes originating from the underlying processes. Thus the different overpotential contributions cannot clearly be distinguished, and it cannot be determined from a single impedance spectrum, how many physically relevant processes the impedance includes.

It is worth to mention that impedance is only defined for systems that satisfy the conditions of linearity and time-invariance. Only a linear or pseudo-linear system results in a sinusoidal phase-shifted response at the same frequency as the sinusoidal perturbation signal. The cell's response is pseudo-linear when the amplitude of the input signal is small and measurements are done in pseudolinear part of the IV curve. Moreover, external factors such as wiring of the current and voltage measurement leads can cause additional capacitive or inductive impedance features in EIS measurements often observed as high and/or low frequency artifacts[6].

## 1.5 Impedance modeling of SOFCs

On an electrochemical level, there are two different model concepts that are frequently used for interpreting impedance spectra: (1) electrical models in the form of equivalent circuits representing physical and chemical processes, and (2) physicochemical models in the form of a microkinetic description of chemical reactions and diffusion processes.

Equivalent circuit modeling is widely employed in electrochemistry in general, and in SOFC literature in particular[7,8,9,10]. Expressions for various circuit elements have been derived from physical laws by early electrochemists, and a detailed introduction is given in MacDonald's classical textbook[11]. It is good enough for an overall performance comparison, but lacks accuracy in explaining the physical source of the different losses, especially due to the usually overlapped arcs of different physiochemical processes. Therefore interpretation in terms of fundamental physical or chemical parameters is often challenging.

Alternatively, impedance can be calculated from a physicochemical model based on an elementary kinetic description of the process. In this approach, the kinetics of the individual reaction steps is expressed in the form of rate equations. Analytical expressions for the impedance of simple electrochemical reaction systems have been given and extended to a variety of systems including SOFCs. Models including diffusive transport were also developed[12,13,14].

A realistic electrochemical system will not only consist of the charge-transfer reaction, but also of some chemical reactions of reactants and products, involving many types of

chemicals and/or charged species. The addition of each species leads to the addition of one differential equation to the rate equation system, and the extension of the right-hand sides with additional terms. Mathematically, this results in a system of differential-algebraic equations (DAE), i.e., a system of ordinary differential equations (ODE) with algebraic restriction equations (e.g., consistency conditions). And to model impedance, the governing equations are typically linearized and the impedance is obtained in the frequency domain after analytical or numerical Fourier transformation.

## 1.6 Complex nonlinear least-squares fitting using equivalent circuits

The impedance simulated and predicted by an equivalent circuit reflects the physicochemical properties of the assumed electrochemical reaction model. If experimental data are available, model parameters can be estimated by varying their values until a best agreement between predicted results and experimental data is obtained. This approach can then directly yield values of physical and chemical properties of the system, including rate coefficients, diffusion coefficients, and other details of the reaction mechanisms.

A fitting procedure called complex nonlinear least-squares fitting (CNLS), was implemented, where data sets of ($Z_{real}$, $Z_{imaginary}$) versus frequency, or (|Z|, phase angle) versus frequency $\omega$ are used. Nonlinear least square fitting is the form of least squares analysis used to fit a set of m observations with a model that is non-linear in n unknown parameters (m > n). It is widely used in the equivalent circuit fitting. The aim of the least squares fitting procedure is to find a set of parameters which will minimize the sum in Equation 1-1.

**Equation 1-1** $$Sum = \sum_{k=1}^{n} w_k \cdot \left[ (Z_{k,r} - Z'_{k,r}(\omega))^2 + (Z_{k,i} - Z'_{k,i}(\omega))^2 \right]$$

Where subscript $k$ denotes the $k$ th data point in impedance plot, $Z_{k,r}$ is the real part of the experimental impedance data, while its counterpart $Z'_{k,r}$ is the theoretical prediction of the real part of the impedance response. Similarly, $Z_{k,i}$ and $Z'_{k,i}$ are the imaginary parts of the impedance, experimentally and theoretically, respectively. Note that the theoretical

prediction of the impedance is a function of frequency $\omega$, which makes fitting of the Nyquist plot actually to be a three dimensional curve fitting. Curves should not only match the correspondence of real and imaginary parts, but also need to match their frequency dependence as well. $w_k$ is the weighting factor, for which we use the magnitude of the $k$ th data point in this study. By minimizing the sum using the least square logarithm, a set of optimized parameters will be obtained.

We chose a Levenberg–Marquardt nonlinear least-squares fitting algorithm because of its straightforward implementation. Any parameter entering the model can in principle be used as a free fitting parameter; however, care must be taken to stay within limits of physical sense. It should also be noted that the Levenberg–Marquardt algorithm does not necessarily iterate to a global optimum of the fitting parameters, nor does it give any indication for the uniqueness of the optimized parameters. Therefore it is important to start from realistic initial guesses for the free parameters, and to exclude fitted results by analyzing its orders of magnitude and looking at the fitted graphs. Or upper and lower bounds can be set in the process of nonlinear least square fitting.

It is worth mentioning that, many research works use predefined equivalent circuits, especially with some constant phase elements, in order to better fit the data. However, it requires 'distributed' elements with power-law frequency exponents such as constant phase elements of capacitance, Gerischer, Warburg, etc., either simply due to the inhomogeneity or from a specific mechanistic origin. And researchers always have the difficulty of getting consistent exponents in the constant phase element, which leaves the electrode reaction mechanism only vaguely or empirically defined, with poor connection between modeling parameters and the properties of the materials. Although such a model may provide a useful set of parameters to 'fit' data accurately, it provides little mechanistic insight. Therefore, if equivalent circuit has to be used, the impedance response of each circuit element needs to have a solid theoretical derivation to support its soundness. In this work, we tried our best to propose an equivalent circuit using the circuit elements which are derived from physically meaningful governing equations to make sure the results can be well-explained and the fitted parameters have a clear and solid physical meaning.

## 1.7 Project background and thesis objectives

The project sponsor Saint-Gobain is trying to fabricate a SOFC stack for commercial purpose, therefore their SOFC team is doing some fundamental research using button cell configuration. One generation of Saint-Gobain's button cell, which they provided to MIT for the specific purpose of this research study and will be called 'Saint-Gobain cell' throughout this thesis, has performance that cannot catch up with the commercially available Julich cell (an anode supported cell with the anode bulk layer to be the main mechanical supporting layer). As can be seen from Figure 1-2 the current produced at the same voltage is much lower in the Saint-Gobain cell (red curve), and Figure 1-3 shows that the resistance of the open circuit AC impedance is also much higher in the Saint-Gobain cell (red curve). From the material point of view, it is hard to understand the difference between the Julich cell and the Saint-Gobain cell because they have very similar design and use the same material (if difference from material preparation can be neglected) and very similar fabrication techniques. Moreover, Figure 1-4 shows a series of AC impedance curve of Saint-Gobain cell when tested for 42 days. It is obvious that the overall resistance of the cell gradually increases as time progresses, and both the area specific resistance and the low frequency arc resistance become larger. In some other degradation testing of the Saint-Gobain cell, significant evolution of the high frequency arc resistance also be observed. This makes the cell performance not as stable as a commercial product should be. Therefore Saint-Gobain really hopes to figure out what limits their cells' performance and lifetime.

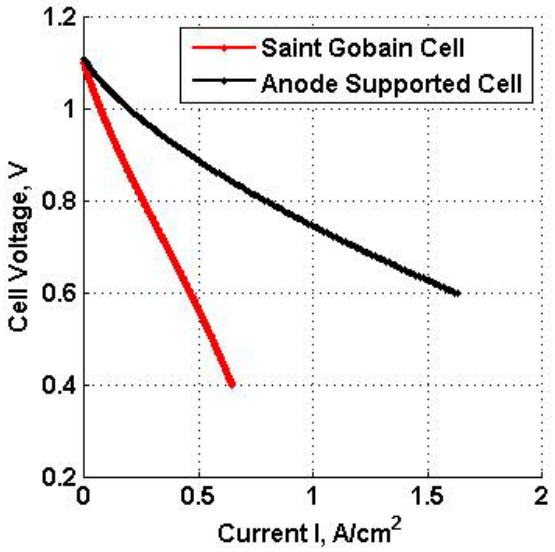


**Figure 1-2 Comparison of the current-voltage (I-V) curves of commercial Julich cell (anode supported cell) and Saint-Gobain cell**

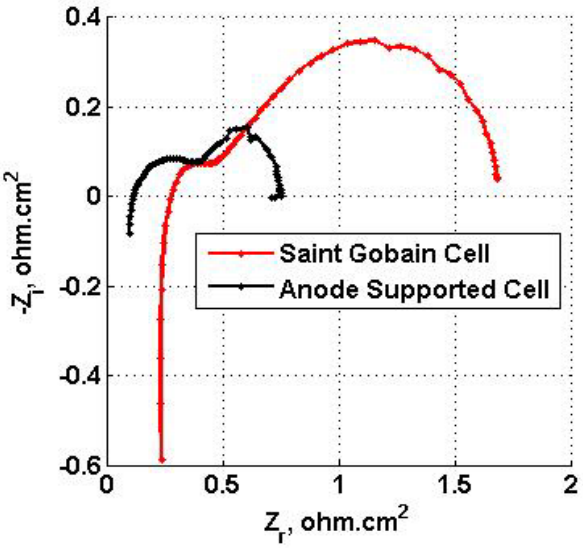


**Figure 1-3 Comparison of the Nyquist plots of commercial Julich cell (anode supported cell) and Saint-Gobain cell**

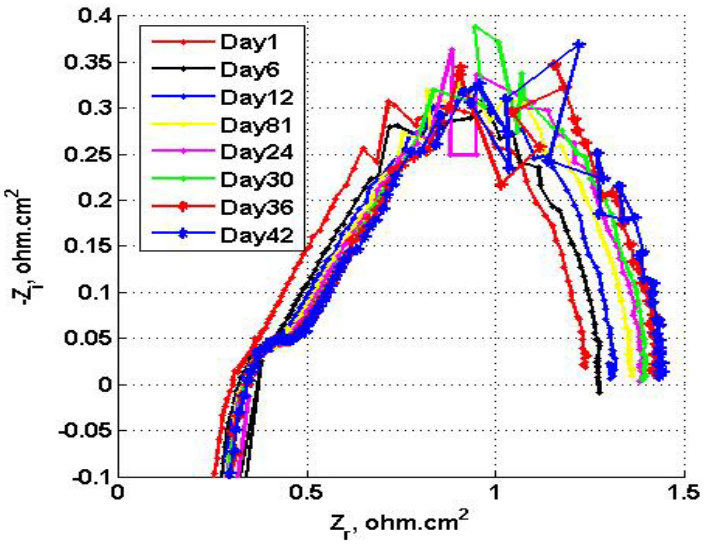


**Figure 1-4 A series of AC impedance curves of a Saint-Gobain button cell when tested for 42 days.**

The SOFC team at Saint-Gobain has implemented a simple 1D button cell model from the literature in Excel to predict the steady state I-V curve, but it has been proven difficult to fit the parameters unambiguously to experimental data and interpret the results in terms of physical properties of the materials or system design that could in principle be optimized. Similarly, the team has measured electrochemical impedance spectra and fitted the data to empirical circuit models, but they have not managed to clearly separate effects of anode and cathode or to extract any meaningful microscopic physical parameters. Instead, all possible polarizations (not only charge transfer, but also mass transfer, at both electrodes, in gas diffusion layers, functional layers and the electrolyte membrane) are lumped into empirical parameters of the area specific resistance 'ASR' and the charge transfer resistance 'Rct', which are not interpreted quantitatively.

It is becoming recognized that a general physics-based model, properly validated against different measurements, would be very helpful in characterizing new materials and optimizing system design. Such a model could allow quantitative prediction of performance and degradation mechanism in button cells. It could explain, e.g., why Saint-Gobain button cells currently do not attain the performance of commercial Julich cells, and how impedance could be used to detect specific degradation mechanisms. A

validated electrochemistry and transport model is also the necessary first step toward performance optimization and scale-up for the full ceramic SOFC stack.

The research of this thesis aims to develop physics-based mathematical models for SOFC. Partial differential equations will be formulated for the transport of mass, coupled to electrochemical reactions in the porous electrodes. The model will be tested and validated against broad range of experimental data for Saint-Gobain button cells and Julich cells, in order to determine the simplest set of equations and parameters that gives a reasonable fit of all of the data. In particular, impedance spectra will be predicted by Fourier analysis of the PDEs and connected to physical parameters, rather than to empirical circuit models. The same parameters can then be used to predict transient current-voltage behavior. By systematically extracting the microscopic physical and electrochemical properties, the model will ultimately be able to guide the performance optimization and scale-up of the SOFC systems. The physics-based model will also provide a rigorous basis for further modeling efforts (at Saint-Gobain and/or MIT) to predict performance and scale-up limitations of the full SOFC stack with ceramic interconnects.

In order to describe certain experiments, the full model will be simplified analytically as needed. For example, to model the impedance, we will linearize the PDEs and apply Fourier analysis to get functional forms to fit to the data, whose parameters are linked clearly to physical variables like reaction rate constants, microstructural properties, geometrical factors, transport coefficients, etc. The resulting impedance models may be possible to interpret as equivalent circuits, such as RC transmission lines and finite length Warburg elements, but the circuit elements would have clear connections to microscopic physical properties.

A crucial goal of this work will be provide a quantitative, physics-based framework to fit and interpret impedance spectra. This will complement, and ideally replace, the empirical fitting methods currently being applied in Saint-Gobain's Northboro research center, e.g., using the 'DRT' (distribution of relaxation times) approach, which is purely mathematical and lacks any microscopic physical basis. By systematically coupling the new model with carefully designed experiments, it should be possible to associate features of the impedance spectra unambiguously with physical processes and parameters.

This will lay the foundation for quantitative interpretation of the data, in particular, to identify the rate determining factor that limit the performance of the Saint-Gobain button cell.

# Chapter 2. Gas diffusion in porous electrode

## 2.1 Introduction

The solid oxide fuel cell is operated with fuel and oxidant being continuously fed from two sides of the cell. Fuel (typically, hydrogen and/or hydrocarbon mixture) is provided to the anode side while oxygen carried by air is provided to the cathode. As the fuel and air react, water vapor is produced and removed from anode. Fuels and oxidants have to be transported through porous electrodes before they arrive at the functional layer, the reaction site. At the same time, product or water vapor has to travel through the porous anode in the opposite direction to be taken away by the flowing stream. Therefore, gas transport through the porous electrode is an essential factor determining the overall cell performance[15,16]. The efficacy of the gas transport through the porous electrodes often determines the rate of electrochemical reaction or current generation.

Furthermore, many researches have shown that the gas transport through porous electrode is mainly governed by gas diffusion with very small convection contribution[17–20]. Thus, diffusion in porous electrode is the main source of concentration polarization (concentration difference between bulk gas and functional layers) in solid oxide fuel cells. However, the diffusion process has not been well understood yet due to 1) gas phase is a multicomponent gas mixture, including reactants, carrier gas and possibly products; 2) the porous electrode, through which gas phase has to travel, could have very complicated microstructures.

There is abundant literature on modeling gas diffusion in porous media using Fick's law, Stefan-Maxwell or Dusty Gas model. It is widely believed that Dusty Gas model is the most accurate and it has already been widely used in numerical simulations[15–17,21,22] (although with constant pressure approximation which is inconsistent[22]). However, very little analytical results are available for these models, especially for the most accurate Dusty Gas model. Also, no theoretical framework is available to analytically derive the

diffusion resistance values from impedance data using these more complex diffusion models for porous media.

Moreover, current researchers usually use limiting current values from the current-voltage (I-V) curves to study gas diffusion in SOFC[23]. Limiting current is usually obtained when the reactant is nearly or completely depleted at the reaction site. Therefore, it has often been used to derive properties of the porous electrode that would account for slow diffusion or sluggish mass transport[23–25]. However, high tortuosity (ratio of actual distance travelled by gas to straight line distance between two points) is commonly invoked to explain the limiting current values. Many previous attempts to fit models to I-V data for SOFC have been inconclusive with widely varying tortuosity values from 2 to 19 for the same system[26–29]. Yet, most direct measurements conducted on anode materials and reconstruction of 3D microstructure indicate tortuosity values should be in the range of 1.5 to 3[30–33]. At the same time, according to the theories about tortuosity[34], we should expect tortuosity of porous electrode with nice and open microstructures to be not too high. Actually, limiting current can have the signature of not only gas diffusion[35], but also dissociative adsorption, surface diffusion, catalytic redox reaction, or even gas transport in free channels outside the electrode. Therefore, we studied gas diffusion in porous electrodes using AC impedance, which better separates processes of different time scales and therefore provides better assignment of arcs in data to different processes.

The SOFC button cell we studied uses hydrogen as fuel, carried by nitrogen together with 1.7% of water vapor, for anode. Oxygen in air is used as oxidant for cathode. Therefore, the electrochemical reaction goes as follows. Oxygen molecule diffuses through cathode bulk layer and reaches the functional layer, where it accepts electrons and is oxidized to oxygen ion, which is further conducted through the electrolyte layer. When it arrives at the anode functional layer, it reacts with hydrogen fuel, forming water and releasing electrons to the external circuit.

In this paper, we present a new theoretical approach to predict concentration profiles and diffusion resistance using Fick's law (Fick), Stefan-Maxwell formulation (SM), and Dusty Gas model (DGM) and compare with experimental data for SOFC. By using this approach in conjunction with AC impedance, we are able to show that DGM provides a

very accurate description of multicomponent gas diffusion and can be used to subtract gas diffusion response from overall data for analyzing contributions from other physical processes.

## 2.2 Theories on gas diffusion in porous media

Transport of gaseous components through porous media has been extensively studied over the years. In general, Models including Fick's model (FM), the Stefan–Maxwell model (SMM) and the Dusty-gas model (DGM) are widely used to predict the concentration overpotential. Many researches have concluded that among the above three, the dusty-gas model is the most accurate and appropriate model to simulate gas transport phenomena inside a porous electrode[17,19,21], such as SOFC electrodes. However, due to its complexity, this model has no analytical solutions, and the corresponding analysis requires complicated numerical simulation[15,16,19,36–38]. In this work, we develop a new theoretical approach which is based on impedance analysis to show how DGM can also been used to analytically analyze the gas diffusion inside the porous media.

### 2.2.1 Fick's law

Fick's law is the simplest diffusion model and is used in dilute or binary systems. It assumes the net flux is proportional to the gradient of the concentration of the corresponding species[39].

**Equation 2-1** $$N_i = -\frac{P}{RT} \cdot D_i^{eff} \frac{dX_i}{dx}$$

$D_i^{eff}$ in Fick's law is the effective diffusion coefficient of species $i$, which takes into account of the composition of the gas mixture. The calculation of $D_i^{eff}$ can be carried out following Equation 2-2. Where $D_i$ is the theoretical diffusion coefficient of species i, $\varepsilon_P$ and $\tau_P$ are the porosity and tortuosity of the porous electrode, respectively.

**Equation 2-2** $D_i^{eff} = D_i \frac{\varepsilon_P}{\tau_P}$

### 2.2.2 Stefan-Maxwell model

Stefan-Maxwell model is more commonly used in multi-component systems because it considers the molecular collisions among different types of the gas species by using a more complicated left hand side term (Equation 2-3)[40–42]. However, it is more typically used for nonporous media. In Equation 2-3, $X_i$ is the mole fraction of species $i$ in the gas mixture, $N_i$ is the mole flux of species $i$, $P$ is total gas pressure in Pa, $R$ is the universal gas constant, $T$ is absolute temperature in K, and $x$ is the 1 D spatial variable.

**Equation 2-3** $$\sum_{j \neq i} \frac{X_j N_i - X_i N_j}{D_{i,j}^{eff}} = -\frac{P}{RT}\frac{dX_i}{dx}$$

### 2.2.3 Dusty Gas model

The Dusty Gas model is an extension of the Stefan-Maxwell equation. It further takes into account the molecules-pore wall interactions by introducing the Knudsen diffusion term (first term in Equation 2-4)[24,38,43]. This model assumes the pore walls consist of large molecules that are uniformly distributed in space. These pseudo or dummy 'dust' molecules also collide with real gas molecules, bringing in the Knudsen diffusion effect.

For the porous material, molecular diffusion is predominant for the case with large pores, whose size is much bigger than the free path of the diffusion gas molecules. The Knudsen diffusion is used when the pores are small in comparison to the mean free path of the gas. In this case, molecules collide more often with the pore walls than with other molecules.

Besides, the viscous fluxes due to pressure gradient are also taken into consideration in DGM. The general form of the DGM is the following (Equation 2-4)

**Equation 2-4** $$\frac{N_i}{D_{K,i}^{eff}} + \sum_{j \neq i} \frac{X_j N_i - X_i N_j}{D_{i,j}^{eff}} = -\frac{P}{RT}\frac{dX_i}{dx} - \frac{X_i}{RT}\left(1 + \frac{1}{D_{K,i}^{eff}}\frac{B_0 P}{\mu}\right)\frac{dP}{dx}$$

where $B_0$ is the permeability of the porous medium and $\mu$ is the viscosity of the gas mixture.

In both SM and DGM, the binary diffusion coefficients $D_{i,j}$ can be calculated by the Chapman-Enskog equation (Equation 2-5) , where $T$ is temperature in K, $p$ is total pressure in Pa, $\Omega$ is the collision integral, $\sigma_{ij}$ is the collision diameter, and $M_i$ is the molecular weight of species $i$[44].

**Equation 2-5** $$D_{i,j} = \frac{1.86\times10^{-3}T^{3/2}\left(\frac{1}{M_i}+\frac{1}{M_j}\right)^{1/2}}{p\Omega\sigma_{ij}^2}$$

The Knudsen diffusion coefficient can be calculated using a kinetic theory that relates the diameter of the pore and the mean free path of the gas, according to Equation 2-6, where $\bar{r}$ is the radius of the gas molecule, $M_i$ is the molecular weight of species $i$[44].

**Equation 2-6** $$D_{K,i} = \frac{2}{3}\left(\frac{8RT}{\pi M_i}\right)^{1/2}\bar{r}$$

Note that this expression was derived from cylindrical pore geometry that having the mean radius. In real porous media, pore geometry can deviate from cylinders, therefore, this expression has some uncertainties in predicting Knudsen diffusivity.

The effective binary diffusivity and Knudsen diffusivity ($D_{i,j}^{eff}$ and $D_{K,i}^{eff}$) were defined as their theoretical counterparts ($D_{i,j}$ and $D_{K,i}$) times a geometric factor, which is porosity ($\varepsilon_P$) divided by tortuosity ($\tau_P$).

**Equation 2-7** $$D_{i,j}^{eff} = D_{i,j}\frac{\varepsilon_P}{\tau_P} \quad and \quad D_{K,i}^{eff} = D_{K,i}\frac{\varepsilon_P}{\tau_P}$$

Numerous studies on transport through porous media in the absence of a chemical reaction reveal that the DGM is superior to the Fick's law in its ability to predict the fluxes. In porous catalyst, the Fick's law is still frequently used because its simplicity

allows explicit and analytical expressions to be derived. If nonuniform pressure is present in a porous media due to reactions involving a change in the number of molecules, additional permeation term has to been taken into account, and therefore DGM should be adopted. Many works[45,46] showed that the DGM can successfully predict the fluxes for these reactions in various reacting systems. For example, Davies[47] used it for the SO2 oxidation reaction, Bliek[48] applied it to the coal gasification where large pressure gradient is present, However, the pressure gradient term requires additional computational time and cost. Therefore researchers started to use DGM without the permeation term if pressure gradient can be approximately neglected. A comparison among different diffusion models, including Fick's Law, Stefan-Maxwell model and Dusty Gas Model, to predict concentration polarization is presented in Suwanwarangkul' work[17].

### 2.2.4 Debates on Graham's law

Interestingly, we found there is a paradox of Dusty Gas model with constant pressure assumption, which has not been widely realized in the community of SOFC. Equation 2-4 shows the general Dusty Gas model with an extra permeation flux term due to the pressure variation, if we sum over all the gas species, the pressure gradient can be calculated as shown in Equation 2-9. By taking a look at the numerator, we can find that the pressure gradient comes from the different effective Knudsen diffusivity $D_{K,i}^{eff}$ of two active species in equi-molar counter-diffusion mode.

**Equation 2-8** $$\sum_i \frac{N_i}{D_{K,i}^{eff}} = -\frac{1}{RT}\left(1+\frac{B_0 P}{\mu}\sum_i \frac{X_i}{D_{K,i}^{eff}}\right)\frac{dP}{dx}$$

**Equation 2-9** $$\frac{dP}{dx} = \frac{-RT\sum_i \frac{N_i}{D_{K,i}^{eff}}}{\left(1+\frac{B_0}{\mu}\sum_i \frac{P\cdot X_i}{D_{K,i}^{eff}}\right)}$$

In the case of hydrogen molecules reacting to produce water vapor, the molar flux of all species should add up to zero. In this equi-molar counter diffusion mode, if the effective Knudsen diffusivity $D_{K,i}^{eff}$ of hydrogen and water are the same, which means if the force exerted on the pore walls by $H_2$ and $H_2O$ are exactly the same but in the opposite

direction, they will cancel each other and no pressure will build up. However, the molecular weight and size of the molecules vary among different species, therefore, Knudsen diffusivity must be different, which means total pressure has to change throughout the electrode.

From another point of view, in the constant pressure assumption, the summation over all gas components will lead to Graham's law[49], which says the sum of molar flux ($N_i$) times the square root of the molecular weight ($M_i$) should add up to zero (Equation 2-10). Actually, the Graham's law is valid in the absence of chemical reactions. But when chemical reactions occur, the component fluxes are related through the reaction stoichiometry, and only isomerization reactions will be consistent with Graham's law.

**Equation 2-10** $\sum_i N_i \sqrt{M_i} = 0$

In our case, moles of $H_2$ react to form equivalent number of moles of $H_2O$ and this is obviously contradictory to the flux relations imposed by the reaction. Since the algebraic derivation from Dusty Gas model to Graham's law is strict, this conflict indicates the Dusty Gas Model is intrinsically inconsistent with the constant pressure assumption. Actually, Graham's law is only valid in the case of gas diffusion without reaction in general. In the case of SOFC, the gas diffusion in porous electrode has a boundary condition of surface reaction at the functional layer/electrolyte interface; therefore, the flux of active species ($H_2$ and $H_2O$) cannot be captured by Graham's law. However, some current researches still use it to study gas transport in porous SOFC electrodes. In fact, full DGM with permeation flux term due to pressure variation has no problem, and is accurate enough to satisfy chemical reaction boundary conditions. Yet with the permeation term, DGM is too complicated for deriving analytical results, therefore restrict its acceptability in some theoretical studies. But we will provide a proof, in section 2.3.3 that in porous electrodes of SOFC, the pressure gradient effects on the gas transport is not significant and can be safely neglected.

## 2.3 Derivation of diffusion resistance $R_b$

### 2.3.1 Steady state

### 2.3.2 Diffusion impedance ($R_b$) (with and without dP)

The above mentioned gas diffusion models, including Fick's law, Stefan Maxwell and Dusty Gas model, are not new, and are widely used to predict I-V curves and fit the limiting current values as mentioned earlier[26,33]. But the SM and DGM models have rarely been used before to analytically analyze impedance spectra of SOFC, although they have been used to describe gas diffusion in porous electrodes. By taking the derivative of the concentration overpotential with respect to current and evaluating it at a specified current, diffusion resistance ($R_b$) is obtained for all three models. By taking a look at zero current $R_b$ in Equation 2-12, Equation 2-13 and Equation 2-14, we notice that compared to $R_b$ value from Fick's law, the $R_b$ of SM has an extra complicated term resulting from the consideration of interactions among different gas species. Also, the $R_b$ value derived from DGM further incorporated the Knudsen effect, which accounts for the collision of gas molecules with the pore wall. The multicomponent gas diffusion inside the porous electrodes was then studied by comparing these three different diffusion models. In Equation 2-11 to Equation 2-14, $R_{b\_anode(I)}$ is the gas diffusion resistance at current I, $\eta_{anode}$ is the anode concentration overpotential due to gas diffusion, $P_i^0$ and $X_i^0$ is the partial pressure and molar fraction of species i in the bulk gas mixture outside the porous electrode. All other parameters are defined the same way as in general Dusty Gas model.

**Equation 2-11** $$R_{b\_anode(I=0)} = \frac{d\eta_{anode}}{dI}_{(I=0)} \quad \text{or} \quad R_{b\_anode(I)} = \frac{d\eta_{anode}}{dI}_{(I)}$$

**Equation 2-12** $$Rb_{Fick(anode)} = \left(\frac{RT}{2F}\right)^2 L_a \left\{ \frac{1}{P_{H2O}^0}\left(\frac{1}{D_{K,H2O}^{eff}} + \frac{1}{D_{H2,H2O}^{eff}}\right) + \frac{1}{P_{H2}^0}\left(\frac{1}{D_{K,H2}^{eff}} + \frac{1}{D_{H2,H2O}^{eff}}\right) \right\}$$

**Equation 2-13**

$$Rb_{SM\,(anode)} = \left(\frac{RT}{2F}\right)^2 L_a \left\{ \begin{array}{l} \frac{1}{P^0_{H2O}} \frac{1}{D^{eff}_{H2,H2O}} + \frac{1}{P^0_{H2}} \frac{1}{D^{eff}_{H2,H2O}} \\ +X^0_{N2}\left(\frac{1}{D^{eff}_{H2,N2}} - \frac{1}{D^{eff}_{N2,H2O}}\right)\cdot\left(\frac{\left(D^{eff}_{H2,H2O} - D^{eff}_{H2O,N2}\right)D^{eff}_{N2,H2}}{\left(D^{eff}_{N2,H2O} - D^{eff}_{H2,N2}\right)D^{eff}_{H2,H2O}P^0_{H2O}} + \frac{\left(D^{eff}_{H2,H2O} - D^{eff}_{H2,N2}\right)D^{eff}_{N2,H2O}}{\left(D^{eff}_{N2,H2O} - D^{eff}_{H2,N2}\right)D^{eff}_{H2,H2O}P^0_{H2}}\right) \end{array} \right\}$$

**Equation 2-14**

$$Rb_{DGM\,(anode)} = \left(\frac{RT}{2F}\right)^2 L_a \left\{ \begin{array}{l} \frac{1}{P^0_{H2O}}\left(\frac{1}{D^{eff}_{K,H2O}} + \frac{1}{D^{eff}_{H2,H2O}}\right) + \frac{1}{P^0_{H2}}\left(\frac{1}{D^{eff}_{K,H2}} + \frac{1}{D^{eff}_{H2,H2O}}\right) \\ +X^0_{N2}\left(\frac{1}{D^{eff}_{H2,N2}} - \frac{1}{D^{eff}_{N2,H2O}}\right)\cdot\left(\frac{\left(D^{eff}_{H2,H2O} - D^{eff}_{H2O,N2}\right)D^{eff}_{N2,H2}}{\left(D^{eff}_{N2,H2O} - D^{eff}_{H2,N2}\right)D^{eff}_{H2,H2O}P^0_{H2O}} + \frac{\left(D^{eff}_{H2,H2O} - D^{eff}_{H2,N2}\right)D^{eff}_{N2,H2O}}{\left(D^{eff}_{N2,H2O} - D^{eff}_{H2,N2}\right)D^{eff}_{H2,H2O}P^0_{H2}}\right) \end{array} \right\}$$

Note that in the $R_b$ expressions, there are not too many quantities that need to be fitted to data. Almost all the variables and parameters are determined from experimental inputs or estimations from kinetic gas theory, except for a microstructure factor (porosity divided by tortuosity), which links effective diffusivity inside porous electrode with its theoretical value. When the porosity is known, then the only quantity need to be determined from fitting is the tortuosity value of the electrodes.

Similarly, cathode diffusion resistance can also be estimated by deriving from a specified diffusion model, e.g., Dusty Gas model derivation was shown in Equation 2-15.

**Equation 2-15** $$Rb_{DGM\,(cathode)} = -\left(\frac{RT}{4F}\right)^2 \frac{L_c}{P^0_{O2}}\left(\frac{1}{D^{eff}_{K,O2}} + \frac{X^0_{N2}}{D^{eff}_{N2,O2}}\right)$$

Comparing the theoretical $R_b$ at anode and cathode, Figure 2-1 shows the ratio between cathode $R_b$ and anode $R_b$ multiplied by 100%. It clearly shows that theoretical $R_b$ of cathode is less than 0.5% of that of the anode in anode supported cells. Though the porosity and tortuosity can be slightly different in two porous electrodes, we can still safely conclude that the diffusion resistance from anode side dominates. Therefore, in all the following discussion, we treat total gas diffusion resistance to be anode gas diffusion resistance, and the low frequency arc in the impedance data was fit with a finite-length Warburg element in a Randles circuit (Figure 2-2) to extract the anode diffusion resistance ($R_b$), which was then compared to analytical predictions from the three diffusion models (Equation 2-12,Equation 2-13,Equation 2-14).

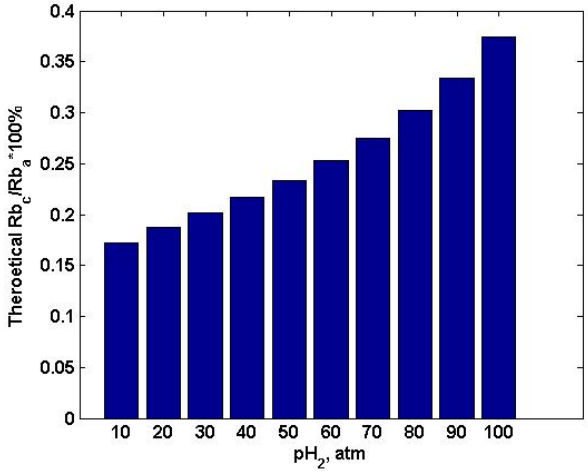


**Figure 2-1 Theoretical comparison of gas diffusion resistance ($R_b$) from cathode and anode in anode supported cell at different $pH_2$ levels.**

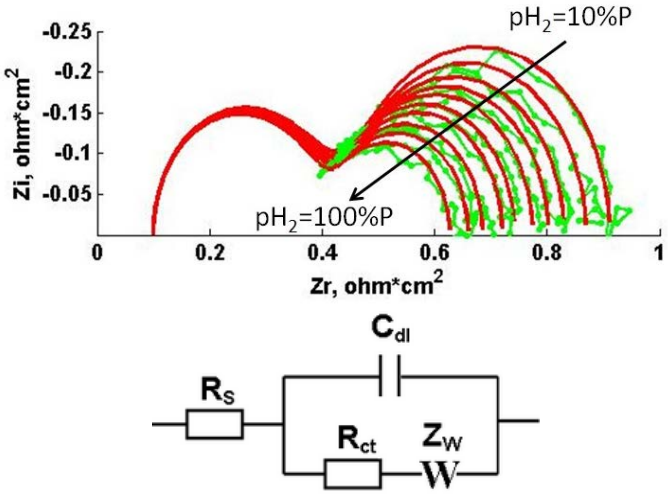


**Figure 2-2 Fitting (top) of the low frequency arcs with the Warburg element in a Randles circuit (bottom).**

### 2.3.3 Proof of using isobaric assumption in Dusty Gas model

As mentioned before, Dusty Gas model is intrinsically inconsistent with isobaric or constant pressure assumption. However, by comparing the gas composition profiles of $H_2$, $N_2$ and $H_2O$, we can see pressure variation only leads to very small deviations of the gas

composition profile (Figure 2-3). At the same time, theoretical prediction of anode gas diffusion resistance $R_b$ values derived from the full Dusty Gas model is practically the same as that derived from the isobaric Dusty Gas model (Figure 2-4). Therefore, our analysis proved that it is still safe to neglect total pressure variation inside the porous electrode when using the Dusty Gas model, although theoretically there is some inconsistency between the model itself and the isobaric assumption. Therefore, all the analysis and results we show in this paper are based on isobaric assumption, assuming total pressure inside porous electrode does not vary in depth.

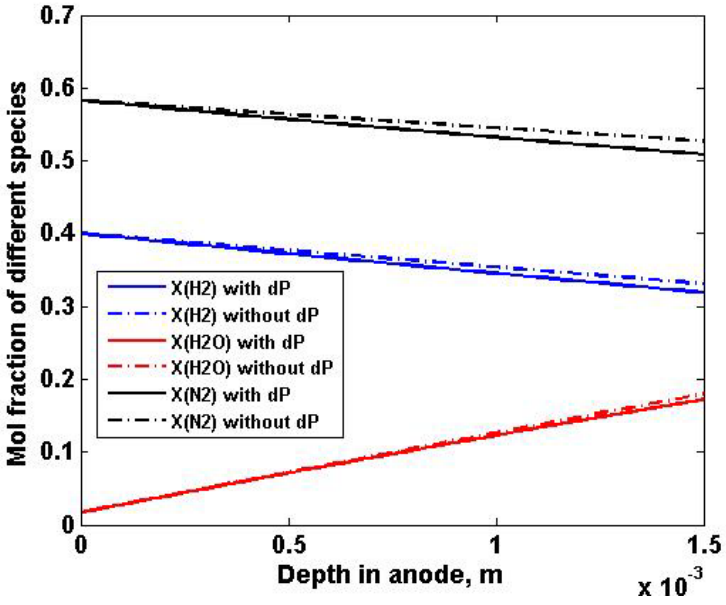


**Figure 2-3 Comparison of anode gas composition profiles under the current of I=100mA (full Dusty Gas model versus isobaric Dusty Gas model)**

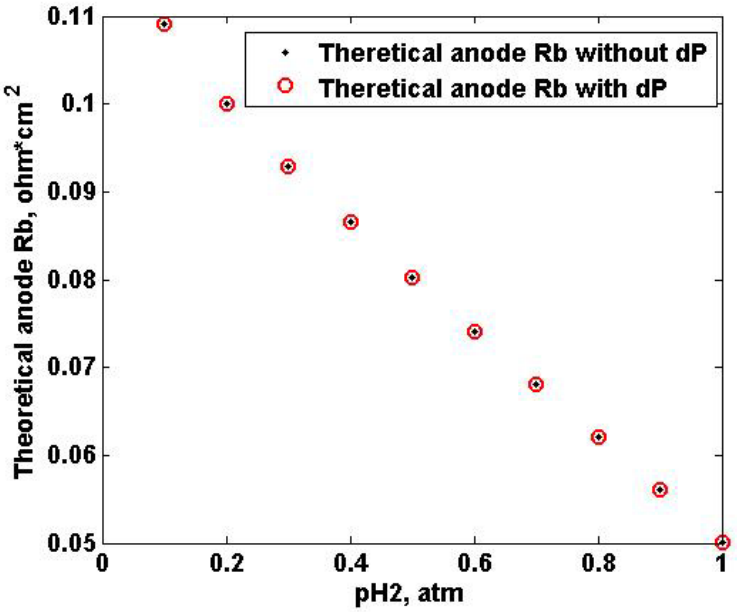


**Figure 2-4 Comparison of theoretical prediction of anode gas diffusion resistance ($R_b$) derived using full Dusty Gas model versus isobaric Dusty Gas model.**

## 2.4 Experiments

Anode-supported single cells were fabricated based on technology developed by Forschungszentrum Jülich. The anode was approximately 1.5 mm thick and 1 inch in diameter, while the cathode was 0.1 mm thick, and 0.5 inch in diameter. The anode side consists of an anode support layer and an anode functional layer with a thickness of 15~30 um, both of which are composed of Ni/YSZ composites with different loadings and microstructures. The cathode side consists of a cathode current collection layer made from pure LSM and a cathode functional layer with a thickness of 15~30 um, which is composed of YSZ/LSM composite.

A new cell was sealed at the circumference using LP-1071 glass from Applied technologies and dried in an oven at 120$^{o}$C for 20 min. Then, it was placed into a spring loaded single cell testing fixture. The fixture was put into a furnace with $N_2$ (150sccm) on the anode side and Air (150sccm) on the cathode side. The furnace was then heated to 800$^{o}$C at 5$^{o}$C/min. The cell was reduced the next morning for 3 hours by gradually switching the anode gas from $N_2$ to $H_2$ flowing at 300 sccm. During testing, a tertiary gas mixture of hydrogen, nitrogen and 3% by volume water vapor was provided to the anode

from a top feeding tube and air was fed from the bottom, carrying oxygen to the cathode. Pt lead wires were connected from the current collector layers (Pt mesh on cathode and nickel on the anode) to the data collecting equipment. A 1470E Solartron Analytical from MTechnologies and mSTAT program were used to control the operating conditions and collect the data.

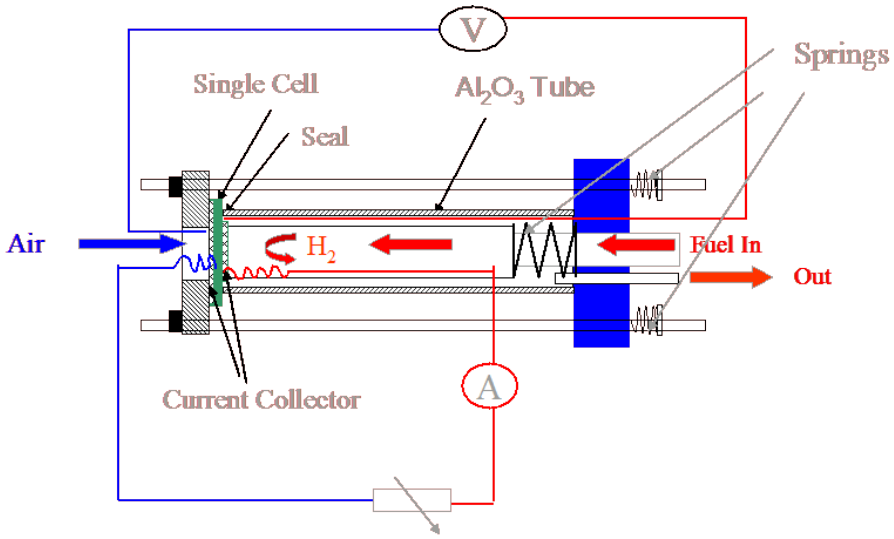


**Figure 2-5 The setup of the spring loaded testing fixture that used for anode supported cell testing.**

AC impedance data of anode-supported cell was collected at open circuit voltage (OCV) condition (Figure 2-6) and 300 mA current (Figure 2-10) when varying the hydrogen partial pressure from 10% to 100% of the total pressure. OCV Impedance data were also collected at three different temperatures (800ºC, 850ºC, and 900ºC) (Figure 2-12).

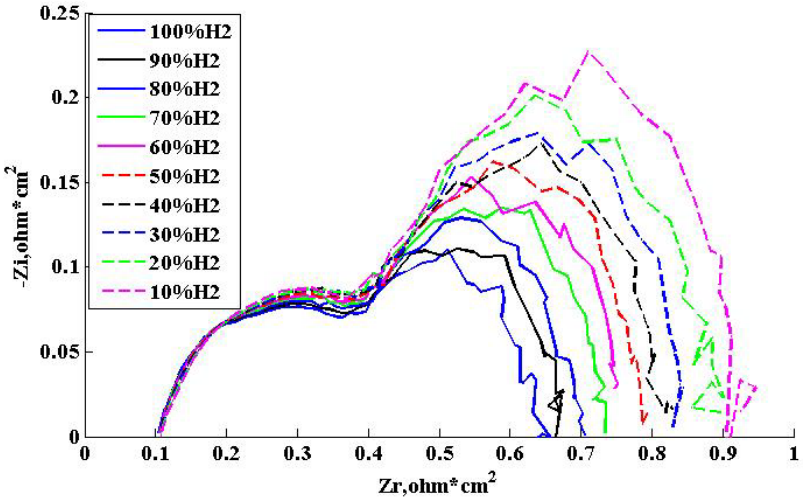


**Figure 2-6 No bias AC impedance data of anode supported cell collected at various hydrogen partial pressures. Total pressure of the anode feeding gas was fixed at 1 atm.**

## 2.5 Results and discussion

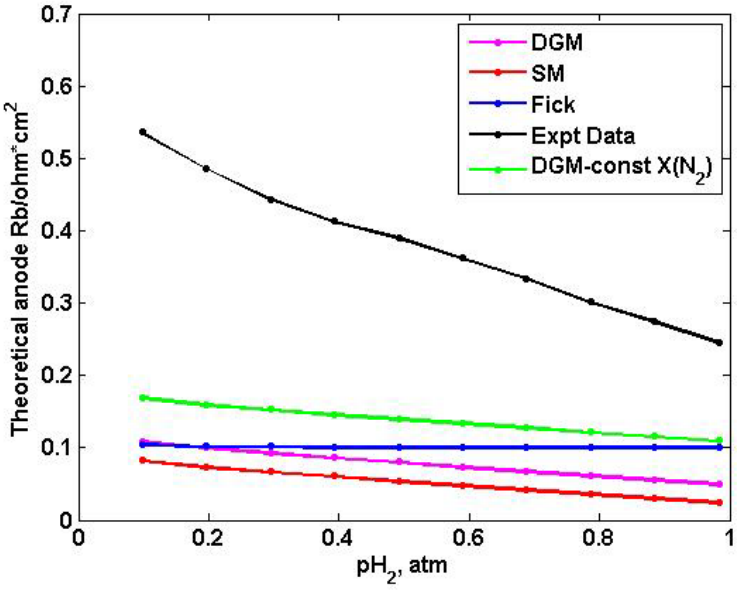


**Figure 2-7 Experimentally extracted anode $R_b$ and theoretical predictions of anode $R_b$ of anode supported cell under different hydrogen partial pressures at OCV.**

Figure 2-7 shows the experimental $R_b$ we extracted from experimental data (black curve), and the theoretical predictions of anode $R_b$ without taking into account the microstructure factor from three different models (colored curves). We also include the anode $R_b$ derived from DGM with an assumption of constant nitrogen composition profile (green curve). By dividing the model prediction to the experimental data, we will be able to obtain the structure factor (porosity divided by tortuosity) from each model.

From the fitting, it is noteworthy that the Dusty Gas model gives a constant structural factor (porosity divided by tortuosity), independent of hydrogen partial pressure (Figure 2-8). This is consistent with real physics, where the microstructure of the porous media does not change with testing conditions. Moreover, with the anode porosity known to be 46%, the tortuosity fitted from the Dusty Gas model is 2.30, which matches both theoretical expectations and direct experimental measurements. After taking into account the fitted tortuosity, the Dusty Gas model best describes the gas diffusion, while the Stefan-Maxwell model shows some deviations, and Fick's law cannot capture the performance at all (Figure 2-9). It is also interesting to note that Dusty Gas model with constant $N_2$ composition does not give good enough results as well, which confirmed the necessity to calculate nitrogen concentration without any assumption, and use it to further calculate concentration profiles of other active species, such as $H_2$ and $H_2O$.

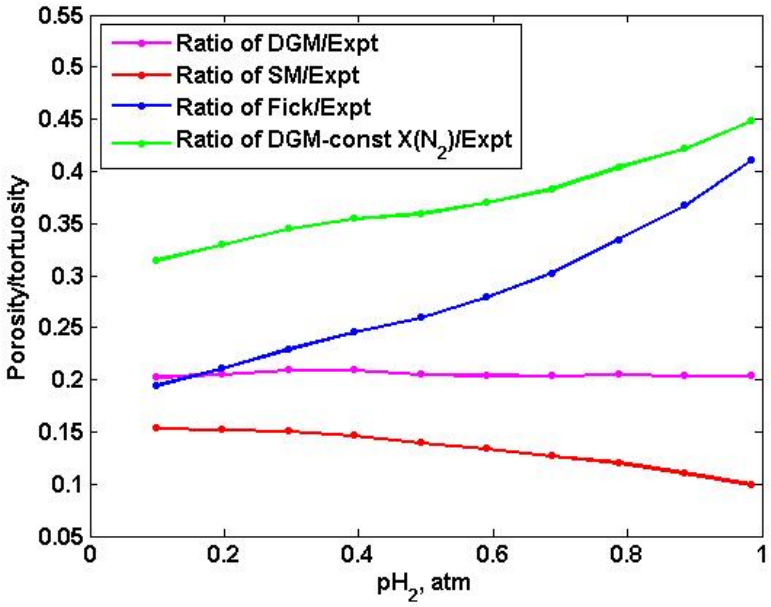


**Figure 2-8 Structural factor (porosity/tortuosity) values fitted from three diffusion models under OCV.**

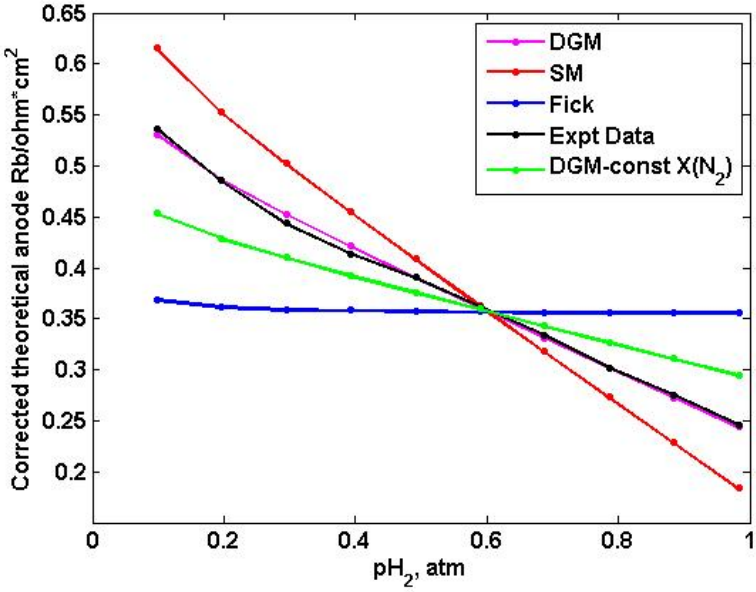


**Figure 2-9 Comparison between diffusion resistances ($R_b$) derived from models and the values extracted from experimental data after taking into account the fitted structural factor (porosity/tortuosity).**

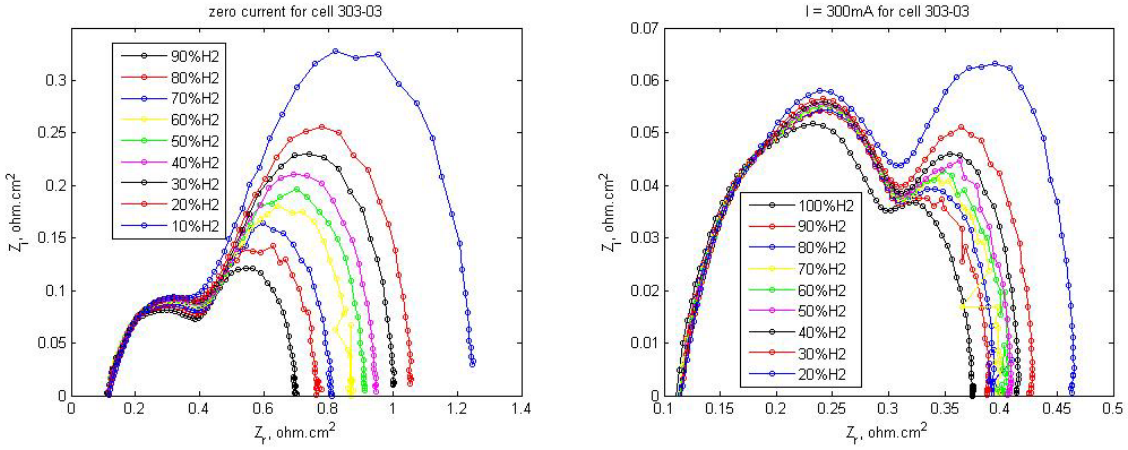


**Figure 2-10 AC impedance data of anode supported cells for anode supported cell (303-03) at OCV (left) and under a current of 300mA, when hydrogen partial pressure is varied.**

We also derived the diffusion resistance $R_b$ for a non-zero current impedance. The impedance was measured at the current of 300 mA/cm$^2$ (Figure 2-10), and the corresponding $R_b$ values for all three models were numerically evaluated using Maple software. It is worth noting that at a non-zero current, the bulk gas concentration (concentration at the interface between porous electrode and gas feeding tube) can deviate from the feeding concentration due to the concentration polarization resulting from consumption of reactants by electrochemical reactions. And, the concentration gradients in the gas feeding tube can be approximated using a continuous stirred tank reactor (CSTR) model. Therefore a CSTR correction (Equation 2-16, Equation 2-17) is introduced for calculating the concentration boundary condition of the bulk gas concentration. $P_i^0$ is the ideal bulk concentration of species $i$, and $P_i^{0*}$ is the corrected bulk concentration of species $i$ after the CSTR formulation.

**Equation 2-16** $$P_{H_2}^{0*} = P_{H_2}^0 - \frac{N_{H_2} A}{m_T} P$$

**Equation 2-17** $$P_{H_2O}^{0*} = P_{H_2O}^0 + \frac{N_{H_2O} A}{m_T} P$$

With the CSTR correction, the fitted porosity/tortuosity is almost independent of feeding gas composition and is practically the same as the zero current impedance analysis, which is another validation of the method of analyzing $R_b$ to extract tortuosity.

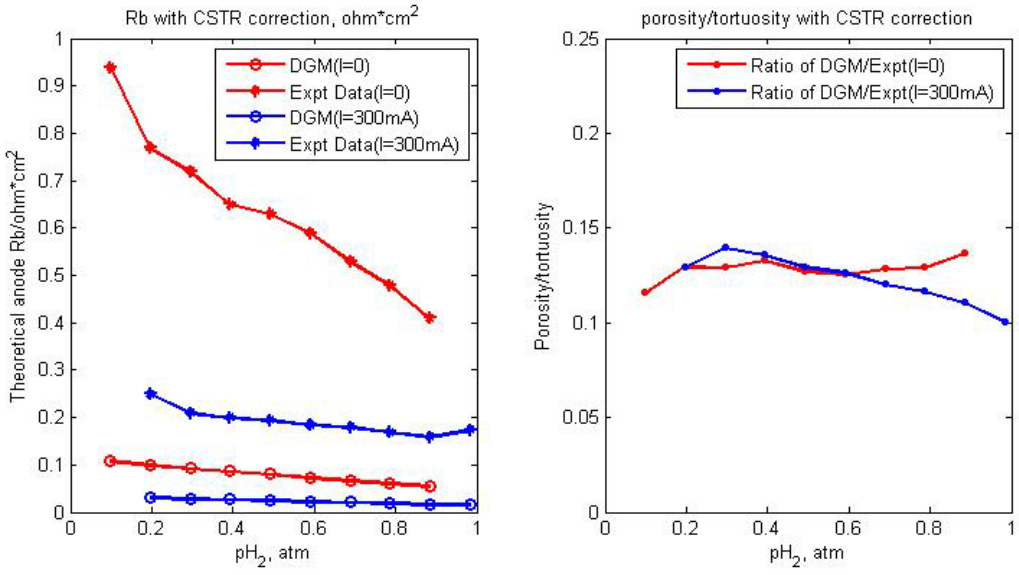


**Figure 2-11 Experimentally extracted anode $R_b$ and theoretical predictions for anode $R_b$ of anode supported cell under different hydrogen partial pressures at both zero and 300 mA/cm$^2$ current, using Dusty Gas model (left). Comparison of the fitted structure factors at two different currents (right).**

We further applied this gas diffusion analysis to zero-current impedance measured at different temperatures (800ºC, 850ºC and 900ºC) (Figure 2-12), and the tortuosity fitted at these temperatures only varies a little, from 3.1 to 3.3 (Figure 2-13). This also shows the applicability of the proposed anode gas diffusion resistance to AC impedance measured at different temperatures.

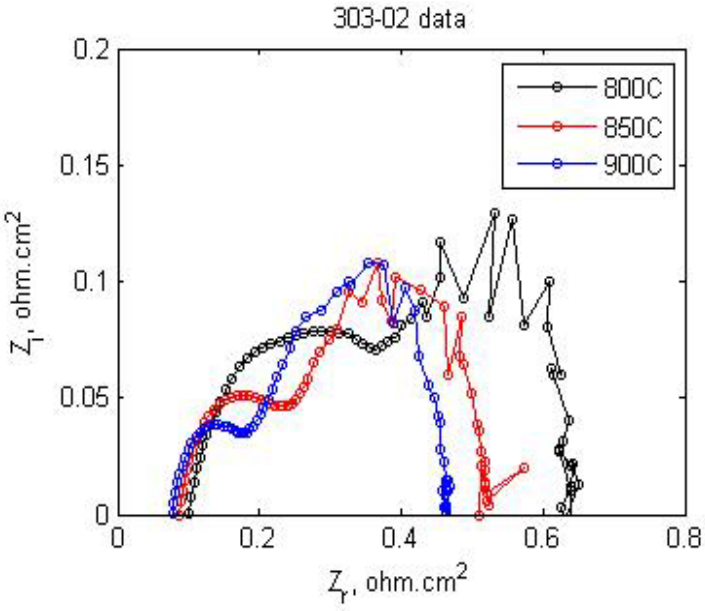


**Figure 2-12 No bias AC impedance data of anode supported cell collected at various temperatures. Hydrogen partial pressure is fixed at 100%, and total pressure of the anode feeding gas was fixed at 1 atm.**

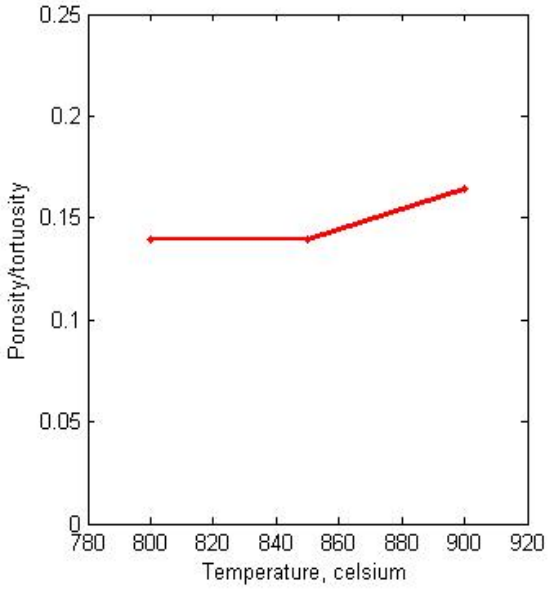


**Figure 2-13 Comparison of the fitted structure factor at three different temperatures (800ºC, 850ºC and 900ºC)**

## 2.6 Conclusion

In this work, we investigated the multi-component gas transport in porous electrodes using anode-supported solid oxide fuel cell, and proposed a new theoretical approach to predict gas diffusion resistance ($R_b$). Explicit analytical expressions for gas diffusion resistance ($R_b$) were derived at zero current conditions, and values of gas diffusion resistance ($R_b$) were evaluated numerically at non-zero current conditions. Comparison of cathode and anode gas diffusion resistance shows that in anode supported cell, anode is the major contributor to gas diffusion resistance.

Experimental $R_b$ values were determined by fitting the low frequency arc of the anode supported cell to the finite length Warburg impedance in a Randles circuit. Then, they were compared to predictions from three analytical models, including Fick's Law, Stefan-Maxwell model, and Dusty Gas model, to determine the structure factor (porosity divided by tortuosity) or tortuosity when porosity is known. An inconsistency between isobaric assumption and the Dusty Gas model was identified, but numerical simulation confirmed that total pressure variation only has very small effects on gas composition profiles and the predicted gas diffusion resistance ($R_b$). Therefore, we can still safely use isobaric assumptions with Dusty Gas model. By incorporating interactions between different gas molecules and collisions between gas molecules and pore walls (Knudsen effect), Dusty Gas model works best and gives a more or less constant tortuosity value over a wide range of operating conditions (10% to ~100% of hydrogen partial pressure, zero and non-zero currents, and three different temperatures), and the fitted tortuosity value matches well with direct experimental measurements.

In summary, this work proposed a new theoretical approach to utilize AC impedance data and Dusty Gas model to analyze multicomponent gas diffusion in porous media. Success of gas diffusion resistance ($R_b$) fitting for a wide range of hydrogen partial pressures, currents and temperatures with single, reasonable tortuosity establishes DGM as the best model for gas diffusion in porous media (at least under these conditions). Therefore, this approach can be used to estimate tortuosity for porous media or to estimate gas diffusion resistance for further investigating other physical processes occurring inside the porous electrodes.

The analysis also shows that impedance is a more reliable method to obtain gas diffusion information inside porous media. It not only better separates processes with different time scales, but also reflects more information on resistances from different processes, therefore enabling the quantitative analysis of gas diffusion in porous media using Dusty Gas Model.

# Chapter 3. Electrocatalysis in porous electrode

## 3.1 Introduction

The term *electrocatalysis* represents a kind of a commingling of two important subdisciplines of physical chemistry, namely, electrochemistry and catalysis. Electrochemistry usually involves electrons and charged chemical species, that need to go over a certain electrochemical potential barrier to make the charge transfer occur. Catalysis is the increase in the rate of a reaction due to the participation of an additional substance called a catalyst. Unlike other reagents in the chemical reaction, a catalyst is not consumed by the reaction. With a catalyst, less free energy is required to reach the transition state, but the total free energy from reactants to products does not change. This definition can be directly extrapolated for electrocatalysis. An electrocatalyst is an electrode material that interacts with some certain species during a Faradaic reaction but still remain unaltered. Since electrode reactions are heterogeneous, electrocatalysts are usually heterogeneous catalysts, which means that an electrocatalytic reaction is usually a multistep heterogeneous reaction, which involves multiple reactants (both charged and uncharged) and several reaction phases (such as gas phase and solid phase, etc). Note that different solid particles are treated as different phases. Typically, it is a multistep process of consecutive adsorption reaction, surface (or bulk) diffusion and charge transfer reaction. If gas phase and solid phase are involved, firstly reactants in the gas phase need to adsorb onto the solid surface, accompanied by some dissociation reaction or electron transfer reactions. This will give some intermediate species (neutral or charged) on the solid surface. Then, these intermediates could either be transported on the solid surface, or enter the bulk lattice of the solid particles, and then be transported to the reactive sites. Either way, they will finally arrive at some active sites where the critical step of the overall reaction (e.g., the charge transfer reaction) would take place. These active sites could locate at a conjunction of three phases, or locate at the interface of two featured phases, depending on different material properties and reaction pathways.

It is very common that different materials, especially different catalysts would lead to different reaction pathways for the same electrocatalytic reaction. Therefore, one needs to specify the system of materials before studying a specific electrocatalytic reaction.

## 3.2 Oxygen reduction reaction at the SOFC cathode

In SOFCs, the cathode (to be more specific, the cathode functional layer) functions as the site for the electrochemical reduction of oxygen. The overall reaction can be written by Kröger – Vink notation as follows:

**Equation 3-1** $\frac{1}{2}O_2(\mathrm{g}) + 2\,\mathrm{e}^- + V_O \longrightarrow O_O^{2-}$

In order for this reaction to occur, three 'species' need to be present: the oxygen gas molecules, electrons and oxygen vacancies in solid phase. Therefore, a material used in the cathode functional layer has to be a good electron conductor, a good oxygen ionic conductor as well as a good gas distributor. Basically there are two categories of materials adopted for this purpose, one is mixed ionic electronic conductor, such as LSCF, which have good ionic and electronic conductivity. The other one is a composite of good ionic conductor (such as yttria-stabilized zirconia (YSZ)) and good electronic conductor (such as lanthanum strontium manganite (LSM)). In both cases, a porous electrode made with micro particles is fabricated in order to make sure the gas can be well delivered into the porous electrode to participate the reaction.

Among many cathode electrode materials for solid oxide fuel cells, LSM is the one of the most heavily pursued material because it provides good electrical and ionic conductivity at elevated temperatures, good thermal and chemical compatibility with YSZ, and relatively high catalytic activity for the ORR[50,51]. With the right choice of Sr content, a nearly exact thermal expansion match between LSM and YSZ can be achieved. Also it is generally more thermodynamically stable than mixed conductors containing cobalt or iron. Therefore, it is a classical cathode material widely adopted in SOFC cathode. However, its ionic conductivity is not high enough for achieving good conduction of the oxygen ions by itself, and the addition of the electrolyte material YSZ to the LSM cathode improves the performance considerably. To optimize the performance of such a

composite electrode, it is important to gain knowledge about mechanism for the electrocatalytic oxygen reduction reaction (ORR) in a porous composite electrode, which is an important phenomenon for SOFCs.

In SOFC, ORR is related to the cathode overpotential at the YSZ/LSM particle interfaces. Since the cathode overpotential is one of the major resistances of SOFCs, it must be minimized to improve performance. For minimizing the cathode resistance, the oxygen transport and reduction reaction mechanism should be clarified around the gas phase/LSM/YSZ interfaces.

Many research works have been conducted about the mechanism of oxygen reduction reaction at the cathode of SOFCs by electrochemical methods with changing the oxygen partial pressure, temperature and applied voltage. It is generally accepted that the oxygen reduction reaction can possibly consist of several elemental steps, following two different pathways. Step 1,2 and 3 is the surface pathway, and step 1,4 and 5 is the bulk pathway. (1) oxygen molecules dissociate and adsorb onto the catalyst surface (e.g., LSM); (2) surface diffusion of oxygen on the catalyst particles; (3) incorporation of oxygen into the electrolyte at the triple phase boundary (TPB) via the surface path (4) oxygen ionic diffusion in the bulk lattice of the catalyst particles; and (5) oxygen ion charge transfer from the catalyst particles to the electrolyte phase (e.g.,YSZ) at the electrolyte/catalyst two phase boundary via the bulk path. One or more of these steps could be the rate-determining in the cathode oxygen reduction reaction. And if more than one of these elementary steps is assumed to be rate limiting, it is hard to analytically derive the overall reaction kinetic expressions, and study needs full numerical simulation to predict the kinetic responses. For simplicity it is often assumed that one of these steps is rate limiting. Moreover, it is also possible for the surface (steps 1,2,3) and bulk (steps 1,4,5) mediated pathways to be present at the same time and compete with each other. Various authors have found different numbers of rate limiting processes[52,53,54,55,56], and the nature of the individual processes is uncertain. Although numerous methods have been developed to measure and describe this reaction, and different rate-limiting reactions have been identified on porous LSM electrodes using EIS, discrepancy still exists in the rate-limiting reactions and associated activation energies[57,58,59–63], and a rigorous framework for connecting kinetic measurements to specific mechanisms has not yet emerged.

Therefore until now, there is no unanimity on the exact details of the cathode electrocatalytic oxygen reduction reaction process in LSM/YSZ system, not even to mention any possible differences introduced by varied materials in SOFC cathode.

Electrochemical analyses suggested some reasonable models for oxygen reduction and/or transports. For example, electrochemical impedance spectra are simulated on the basis of a model representing physical conservation laws for porous-media transport and elementary chemistry for an internal reforming in fuel cell in Zhu's work[28]. The study used a reaction mechanism which assumes one of the charge transfer elementary steps is rate limiting, and have reasonably well fitted the experimental data. The modified Butler-Volmer reaction is derived in his previous work in 2005[64] and was adopted by many other researchers as well. Hofmann also presented a successful implementation of a dynamic planar SOFC model with its special feature of its capability to simulate electrochemical impedance spectroscopy (EIS). However, in these types of models, there are usually many fitting parameters, and the exchange current density and charge transfer coefficient values are always of great uncertainty.

In the early stage of modeling the SOFC cathode, the charge transfer limited kinetics was generally adopted. However, Adler and other researchers pointed out that even though the phenomenal responses of the system follows Butler-Volmer type expression, it may not necessarily imply that the charge transfer is rate limiting[65,66]. Indeed, the electrode kinetics can be explained solely in terms of the transport and chemical-kinetic properties of the mixed conductor, with all charge transfer steps assumed to be equilibrated. Researchers began to wonder if any surface process could be slower than charge transfer in the LSM/YSZ system. Some works have demonstrated that electrodes with I-V characteristics indicative of charge-transfer limitations (e.g. Tafel behavior) can in fact be limited by steps that do not involve charge-transfer[67].

For the system of LSM/YSZ, the electrode kinetics seems to be complicated. Evidence suggests that oxygen absorption and transport in the surface or/and bulk of the LSM particles may play a significant (if not dominant) role in determining the electrode polarization. Several publications show that thin film electrodes and particularly microstructured thin film electrodes are often more favorable than porous electrodes for

detailed mechanistic investigation of polarization processes at SOFC electrode materials[68,69,70,71,72]. Geometry dependent measurements on LSM microelectrodes revealed that not only the oxygen reduction via the triple phase boundary but also the bulk path with oxygen incorporation into the LSM and ion transport through LSM contributes to the overall current[57,73,69,70]. Other works also favor the surface mediated pathway. Van Heuveln reported that the diffusion of $O_2$ species along the LSM surface to the TPB area competes with charge transfer, and is the rate-determining step at low overpotential[74,75]. Ostergard and Mogensen proposed three rate-limiting steps, which include dissociative adsorption of oxygen, diffusion of oxygen ions to the interface, and transfer of oxygen ions from the interface to the oxygen ion vacancies inside the electrolyte, and suggested that the dissociative adsorption may be a rate-determining step under typical reaction conditions[6]. This was supported by Siebert, who suggested that the rate-determining step of the oxygen reduction reaction on LSM at low overpotential is dissociative adsorption[57]. Wang suggested that intermediate frequency arcs in cathode impedance response are related to the dissociative adsorption of $O_2$[76]. Shao-Horn also studied EIS of dense, thin-film microelectrodes and pointed that the overall ORR rate may be limited by mixed bulk/TPB charge transfer processes below 700°C and surface chemical reactions above 700°C[72].

In the works related to ORR mechanism, some found that the kinetics are proportional to the TPB length per electrode area[7,77,78], while others found they are proportional to the contact area between YSZ and LSM, and the electrode performance depends more on bulk transport phenomena[57,79,69].

In the former case, it is possible that the reaction is co-limited by adsorption and surface diffusion, or the reaction could also be limited by electrochemical kinetics at the TPB itself. Both situations and a combination thereof would result in the resistance scaling with the reciprocal of the TPB length. Another possibility is that the reaction is limited by mechanisms acting farther away from the TPB but which scale with electrode geometric factors that are strongly correlated to the length of the TPB (for example, through the process of sintering). In the latter case when kinetics is proportional to the contact area between YSZ and LSM, it is highly possible that the reaction is limited by some step, possibly the incorporation of oxygen ion that occurs at the YSZ/LSM two phase

boundary. Some researchers also claimed that even if the charge transfer reaction tends to occur at the TPB, it may also occur in an extended area near the TPB. One typical work in the pattern cathode area is conducted by Horita et al[68], who used isotope oxygen exchange ($^{16}O/^{18}O$ exchange) and secondary ion mass spectrometry analysis (SIMS) on LSM-mesh cathode to visualize the kinetics of oxygen transport. Their results showed the extension of TPB by measuring the isotope oxygen responses in the patterned electrode. They also showed the LSM-mesh/YSZ interface is active for oxygen incorporation, and the active sites for oxygen incorporation were distributed at the surface which confirms that some amounts of oxygen can diffuse via the oxygen vacancy in LSM.

Actually, there are many factors making studies in this area challenging: 1) The LSM particle properties vary a lot depending on how it was prepared and used in the fabrication of the cathode layer; 2) material properties of the LSM vary with the applied overpotential. The oxygen vacancy concentration would increase at higher cathodic overpotenial, and therefore make the oxygen bulk diffusivity increase at higher currents[72]; 3) microstructure of the composite cathode electrode, especially how much triple phase boundary is present, and how each phase is connected, can greatly affect the reaction kinetics, and thus the cell performance; 4) even if a reaction mechanism is determined for a certain electrode, e.g., patterned LSM/YSZ electrode, it may not be applicable for the porous composite electrode[80]; 5) it is possible that the overall reaction kinetics have more than one rate determining step, and also more than one pathway which are competitive to each other. 6) the electrode kinetics are very dependent on the polarization history in SOFCs. Thus, it is difficult to say whether two cells operating at the same current density are really at the same operating point. Therefore, it is very difficult to correlate the complex electrochemical characteristics of LSM to the highly complex microstructure of a porous electrode.

In summary, the challenges in the study of the reaction mechanism of catalytic oxygen reduction reaction at the cathode of solid oxide fuel cell are many factors that may greatly affect the reaction mechanism, especially when parallel pathways are present, including LSM composition, surface property, porous electrode microstructure, YSZ/LSM loading ratio, particle size, and operating conditions, etc. This makes it worthwhile to study a specific system even though large quantities of literature papers are available. In this

research, we started with modeling the surface mediated path which, according to literature reports[6,74,75], seems reasonable for the case of low overpotential at around 800°C.

## 3.3 Gerischer element

As described above, the electrocatalytic reaction usually contain both chemical reaction and diffusion process (either bulk diffusion or surface diffusion). This diffusion-reaction system is typical in chemical engineering, and its impedance response has been studied and derived by early researchers.

In 1951, Gerischer[81] published the formal treatment of the DC and AC response for a reaction of the type of a chemical reaction followed by an electrochemical one, at an inert electrode in an aqueous electrolyte. The governing equation of this process can be described as Equation 3-2.

**Equation 3-2** $$\frac{\partial c}{\partial t} = D\frac{\partial^2 c}{\partial x^2} + k \cdot c$$

In Equation 3-1, $c$ is the concentration of the reactant, and $D$ is the diffusion coefficient, and the last term $k \cdot c$ is the reaction term, assuming the pseudo first order irreversible reaction, and $k$ is the effective kinetic rate constant for this reaction term. Based on the reaction direction, $k$ can be positive or negative, making this term as source or sink in addition to the diffusion process.

Almost two decades later, Sluyters-Rehbach and Sluyters[82] presented the general impedance expression for a similar reaction-diffusion system, which was aptly named the 'Gerischer' impedance. In 1984, they also published the complete impedance expression for an electrochemical reaction preceded and followed by a chemical reaction[83]. Under special conditions of infinite large $\frac{k+i\omega}{D}$, the hyperbolic tanh function goes to 1 and therefore the complex expression reduces to a quite simple impedance relation of Equation 3-3.

**Equation 3-3** $Z_{(\omega)} = \frac{Z_0}{\sqrt{k + i\omega}}$

Here, $k$ represents the effective transfer rate of the chemical reaction, and the boundary condition applied at a large distance is the fixed concentration, assuming an infinitely large reservoir. Therefore, it is not the real case for the fuel cell case. There are some papers studying diffusion plus gas adsorption type reactions for the SOFC cathode materials, but as far as we known, there is not a specific paper studying LSM/YSZ cathode giving out a theoretical derivation of impedance response that uses symmetric boundary condition (or called 'reflecting boundary condition') as well as Langmuir adsorption kinetics. Since the concept of diffusion plus reaction is a typical chemical engineering problem, we will not be surprised if similar problem has been solved and reported somewhere in other related areas.

J. Bisquert[84] studied the similar physical process in another application, with governing equations describing the kinetics of ion diffusion and trapping in intercalation materials. Though the diffusion process is bulk diffusion inside solid particles, the fundamentals are similar to what occurs in porous composite cathode of the solid oxide fuel cells. J.P. Diard[85] studied the hydrogen diffusion-trapping in metals and alloys, as well as ion insertion-trapping in host materials, and also gave an analytical expression for a diffusion-trapping controlled processes studied under restricted linear diffusion conditions. Interestingly, both of their derived analytical impedance expression is in the similar form as ours (Equation 3-13), with a coth term. This similarity further corroborated our analysis for the surface reaction-diffusion system with a symmetry boundary condition. In fact we developed the following model for impedance response of the surface diffusion and adsorption process independently before we found the above papers, and the unique part of our work is the 'surface' process, which makes the impedance have a volcano shaped dependence of the thermodynamic constant K or $pO_2$, as will be discussed in section 3.5.2.

## 3.4 Model development for the electrocatalysis in SOFC cathode

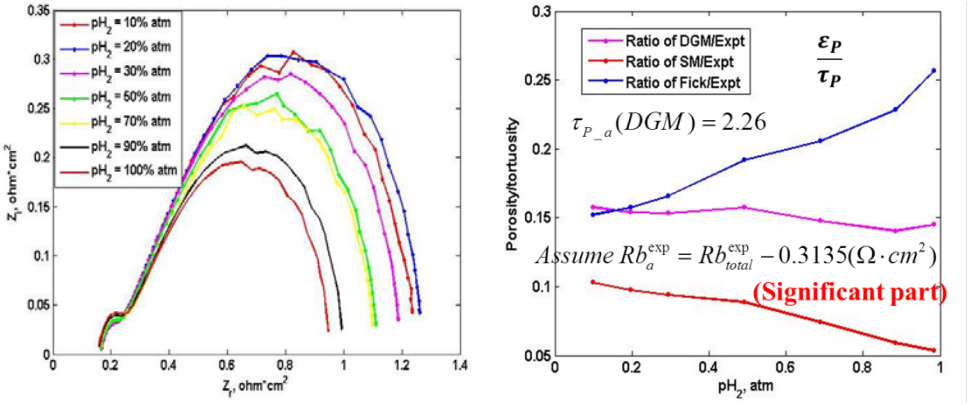


**Figure 3-1 (Left) No bias AC impedance of a Saint-Gobain cell measured at 800ºC, when hydrogen partial pressure is varied. (Right) An extra resistance has to been removed to make the gas diffusion resistance calculation reasonable.**

When no bias AC impedance measured at 800ºC were measured for Saint-Gobain cell as hydrogen partial pressure varies, we can extract the anode gas diffusion resistance information from the data. A similar gas diffusion analysis shows that, compared to the anode supported cell, a significant extra resistance has to been removed in order to make the gas diffusion resistance calculation reasonable (Figure 3-1), that is predicting an almost constant tortuosity values for different partial pressure conditions.

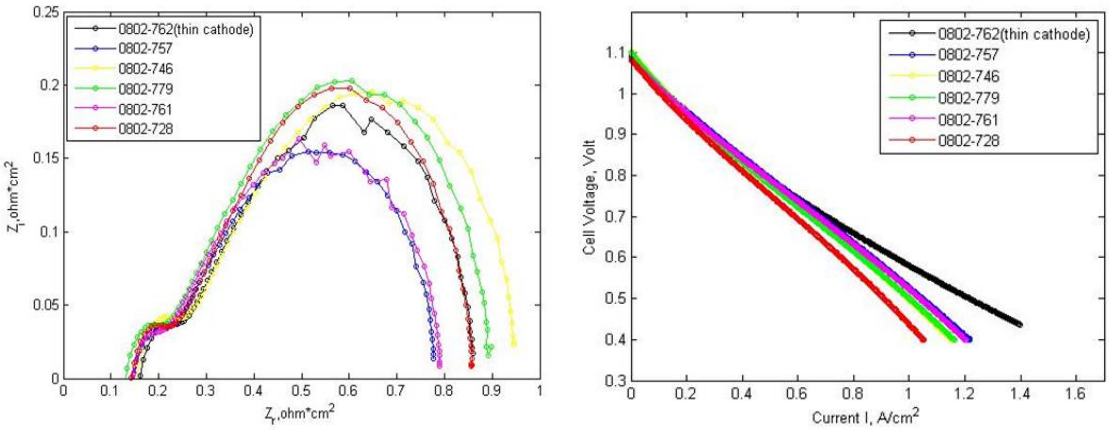


**Figure 3-2 No bias AC impedance and IV curves comparison between normal Saint Gobain cells and a cell with thinner cathode supporting layer (0802-762).**

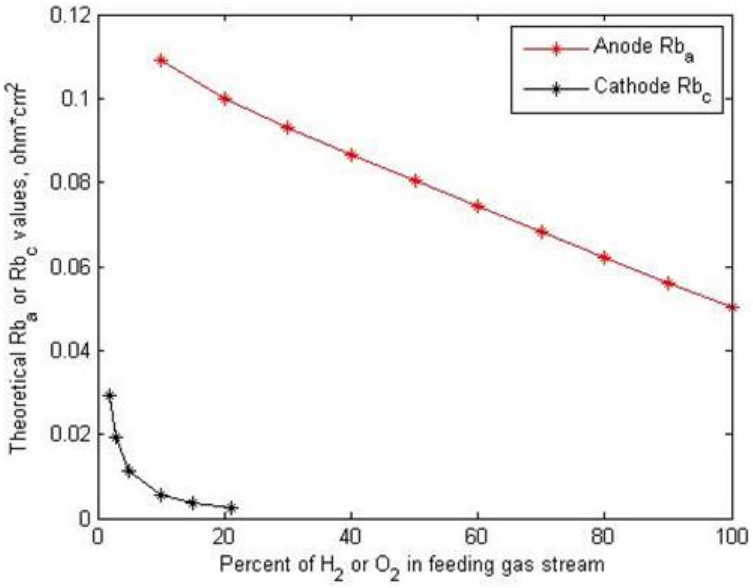


**Figure 3-3 A theoretical comparison between anode and cathode gas diffusion resistance at the corresponding supporting layer, assuing both are 1500um thick.**

Then we questioned the sources of this extra resistance. A cell with much thinner cathode supporting layer (100um versus 1200um in normal cells) was fabricated, and no bias AC impedance and current-voltage (I-V) curves were compared. Data shows that the thinner cathode supporting layer does not have obvious performance difference compared to normal Saint-Gobain cells. A theoretical analysis to estimate the gas diffusion resistance at the cathode supporting layer was also carried out (Figure 3-3). It shows that even if we assume that the cathode supporting layer is of the same thickness as the anode (e.g., 1500um), the gas diffusion resistance at the cathode side is still much smaller than that of the anode side (<5%). Therefore, the extra resistance we identified at the cathode side is not due to the gas diffusion. It must come from other processes at the cathode.

As mentioned above, the low frequency arc of Saint-Gobain cells contain some contributions from the cathode, but not due to cathode gas diffusion process. Therefore, it must come from some other cathode processes, such as gas adsorption, surface diffusion on catalytic particles or bulk diffusion inside solid catalytic particles, etc. In this chapter, we developed a model to describe the catalytic oxygen reduction reaction at the cathode functional layer. Symmetric cathode cells were fabricated and no bias impedance was

measured under different oxygen gas partial pressures $pO_2$ so that any anode contribution can be eliminated. In the model development, we started with a simple case which assumes that the surface path dominates, and bulk path (which is highly possible to kick in at high overpotential) is somewhat suppressed at the low overpotential.

We set up a model for cathode surface process which describes both oxygen adsorption and intermediate surface diffusion. The catalytic surface process is demonstrated in Figure 3-4. Gas phase oxygen molecules dissociate and adsorb onto the surface of LSM particles, and then diffuse on the LSM surface to the triple phase boundary (TPB) where all three phases (LSM, YSZ and the gas phase) meet and the charge transfer reaction occurs. The adsorption and surface diffusion occur simultaneously along the LSM surface, and it is hard to assume in prior which process would be rate limiting. Therefore, the model has to describe a process which is co-limited by gas adsorption on catalyst (LSM) surface and surface diffusion. The characteristic length of the overall surface adsorption-diffusion process is defined as $L_s$, which we call it surface diffusion length. It is typically the half distance between two TPB points along the LSM surface. Then there is another boundary layer thickness $l_\delta$, and the surface diffusion process mainly occurs close to TPB within this boundary layer thickness. The importance of relativeness of these two lengths will be discussed in section 3.5.2.

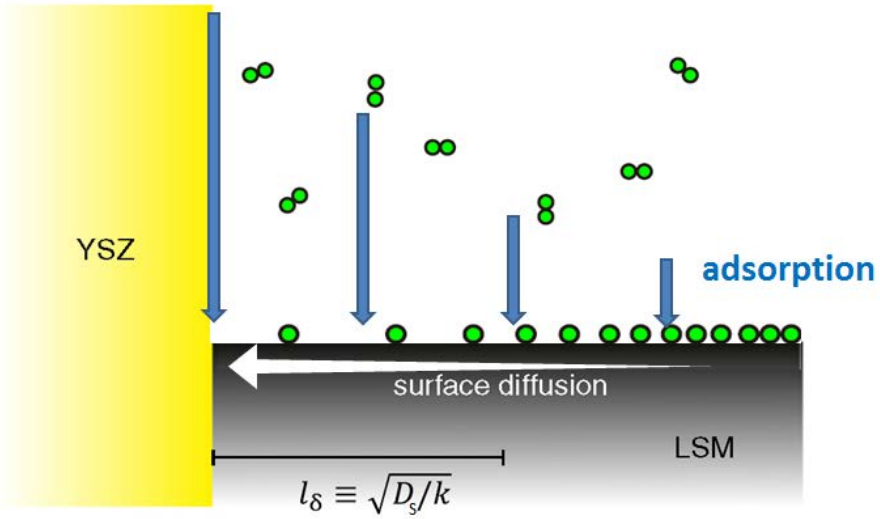

**Figure 3-4. Electrocatalytic kinetic process of LSM/YSZ porous electrode co-limited by surface diffusion and adsorption respectively. Picture modified from E-C Shin's 2013 paper[86].**

In the case of heterogeneous reactions taking place at an electrode surface, adsorption and desorption reactions will be important sources or sinks for the involved species. The governing equation for surface coverage in this process is shown below when absorption process is described by Langmuir kinetics. Oxygen molecule is a two atoms molecule, so the number of sites required for one molecule to absorb is two. Similarly it requires two of the adsorbed oxygen atoms to desorb and combine to an oxygen gas molecule. This makes the forward and backward reaction rate in the adsorption term (sink/source term) proportional to the square of fraction of surface vacancy and square of surface coverage, respectively. (Equation 3-4)

**Equation 3-4** $$\frac{\partial \theta}{\partial t} = D_s \frac{\partial^2 \theta}{\partial x^2} + k_{ads}\left(K \cdot P_{O_2}(1-\theta)^2 - \theta^2\right)$$

In this equation, $\theta$ is the non-dimentionalized surface coverage between 0 and 1. $D_s$ is the surface (or surface mixed with solid bulk) diffusivity. $k_{ads}$ is the kinetic constant of the Langmuir adsorption process, and $K$ is the thermodynamic equilibrium constant for the adsorption of $O_2$ onto LSM surface.

When a sinusoidal external signal is applied, the surface coverage can be expressed as $\theta = \theta_{eq} e^{i \cdot \omega \cdot t}$, therefore the time derivative term can be replaced by $i \cdot \omega \cdot \theta$. And under small perturbation, we can assume the surface coverage is a steady state profile disturbed by a small surface concentration (coverage) change ( $\theta_{tot} = \theta_{eq} + \Delta\theta$ ), therefore the equation can be linearized to be Equation 3-6:

**Equation 3-5** $$\frac{\partial(\theta_{eq} + \Delta\theta)}{\partial t} = D_s \frac{\partial^2(\theta_{eq} + \Delta\theta)}{\partial x^2} + k_{ads}\left(K \cdot P_{O_2}(1-(\theta_{eq} + \Delta\theta))^2 - (\theta_{eq} + \Delta\theta)^2\right)$$

**Equation 3-6** $$i \cdot \omega \cdot \Delta\theta = D_s \frac{\partial^2 \Delta\theta}{\partial x^2} + 2k_{ads}\left(K \cdot P_{O_2}(\theta_{eq} - 1) - \theta_{eq}\right)\Delta\theta$$

When impedance is measured at open circuit voltage (no bias impedance), spatial derivative of $\theta$ disappears as well. Therefore the equilibrium coverage $\theta_{eq}$ is the coverage when Langmuir adsorption reaches equilibrium.

**Equation 3-7** $\theta_{eq} = \frac{\sqrt{K \cdot P_{O_2}}}{1+\sqrt{K \cdot P_{O_2}}}$

Thus Equation 3-6 can be rewritten as

**Equation 3-8** $i \cdot \omega \cdot \Delta\theta = D_s \frac{\partial^2 \Delta\theta}{\partial x^2} - k \cdot \Delta\theta \qquad where\ \ k = 2 \cdot k_{ads} \cdot \sqrt{K \cdot P_{O_2}}$

We use a symmetry boundary condition for x= $L_s$, since the triple phase boundary is distributed randomly inside the functional layer. It is most likely that adsorption occurs on the surface of catalytic LSM particles and then adsorbed species diffuse to TPB available in different directions. Therefore, adsorption process is most likely to achieve equilibrium in the place that is the farthest away from TPB. And no matter whether adsorption reaches equilibrium or not, in the middle region a no gradient boundary condition can be applied (in 1D case). Then the equation can be solved analytically as shown in Equation 3-9, and AC impedance response can be calculated (Equation 3-13).

**Equation 3-9** $\Delta\theta = q \cdot \exp\left(\sqrt{\frac{i \cdot \omega + k}{D_s}} L_s\right) \cosh\left(\sqrt{\frac{i \cdot \omega + k}{D_s}} \left(L_s - x\right)\right)$

Where q is a constant prefactor restricted by the boundary condition at x=0.

**Equation 3-10** $V = V^{\Theta} + \frac{k \cdot T}{n \cdot e} \ln \frac{\theta}{1-\theta}$

According to the Nernst equation (Equation 3-10), voltage perturbation can be expressed as in Equation 3-11 (detailed derivation can be found in appendix of this chapter), and the current perturbation per area can also be expressed according to its physical meaning (Equation 3-12), where $l_{TPB}$ is the triple phase boundary density per electrode area, $n$ is the number of electrons involved in the process, $e$ is the unit charge, $N_A$ is the Avogadro constant, $D_s$ is the diffusivity of this diffusion process (could be purely surface diffusion

or a combination of both surface and bulk diffusion). $C_{\max}$ is the maximum concentration of surface sites on the catalytic particles (LSM).

**Equation 3-11** $\Delta V = \frac{R \cdot T}{n \cdot F} \frac{\Delta\theta}{\theta^{eq}\left(1-\theta^{eq}\right)}$

**Equation 3-12** $\Delta I = l_{TPB} \cdot n \cdot e \cdot N_A \cdot D_s \cdot C_{\max} \frac{\partial \Delta\theta}{\partial x}$

Then, the impedance response of this cathode process can be obtained by dividing voltage perturbation by current perturbation, as shown in Equation 3-13. Note that compared to the traditional Gerischer impedance expression with a tanh term, here due to the symmetric no gradient boundary condition we used at x= $L_s$ , the impedance is proportional to a coth term. Again, the effective transfer rate of the oxygen adsorption rate is a function of oxygen partial pressure $pO_2$, as well as the other Langmuir adsorption parameters: $k = 2 \cdot k_{ads} \cdot \sqrt{K \cdot P_{O_2}}$ .

**Equation 3-13** $Z_G = \frac{\Delta V}{\Delta I} = \frac{RT}{(n \cdot F)^2} \frac{1}{l_{TPB} \cdot D_s \cdot C_{\max}} \left( 2 + \frac{1}{\sqrt{K \cdot P_{O_2}}} + \sqrt{K \cdot P_{O_2}} \right) \frac{\coth\left( \sqrt{\frac{i \cdot \omega + k}{D_s}} L_s \right)}{\sqrt{\frac{i \cdot \omega + k}{D_s}}}$

Note that in this derivation we assumed uniform overpotential across the whole cathode functional layer, but in real operation conditions (especially when a large current is being drawn) there might be a distribution of overpotential across the functional layer, that is, the reaction rate closer to the electrolyte is larger compared to the position that is closer to the cathode current collector. Therefore, if necessary, one can also derive the analytical impedance results for a nonuniform overpotential.

## 3.5 Validation of the cathode electrocatalysis model

### 3.5.1 Frequency and $pO_2$ dependence

After we derived the theoretical impedance response for the cathode process which is co-limited by oxygen adsorption and surface diffusion, we proposed an equivalent circuit as shown in Figure 3-5. The inductor L1 accounts for the inductance effects from the long

lead wire needed for the high temperature measurements. The necessity for including this inductance is shown in E-C.Shin's paper[86]. In our work, since we only have a long tail in the fourth quadrant in parallel with imaginary axis, only inductance is necessary to explain it. Resistance R1 represents the total ohmic resistance of the symmetric cathode cell, mainly coming from the electrolyte ohmic resistance and other contact resistances. The R2 and C1 in parallel (called $R_F$ and $C_F$ in fitting results) accounts for the reactions associated with high frequency arc. In this symmetric cathode cell, it only represents the cathode charge transfer reaction. Finally, the cathode surface process is represented by an element GE1, whose impedance response was analytically derived in this research. Since we have two cathodes, R2,C1 and the GE1 element need to be multiplied by two when fitting the symmetric cathode data.

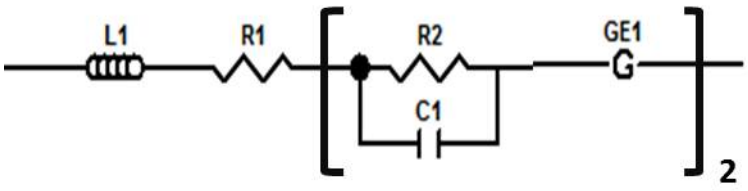


**Figure 3-5 Physics based equivalent model for the symmetric cathode cells.**

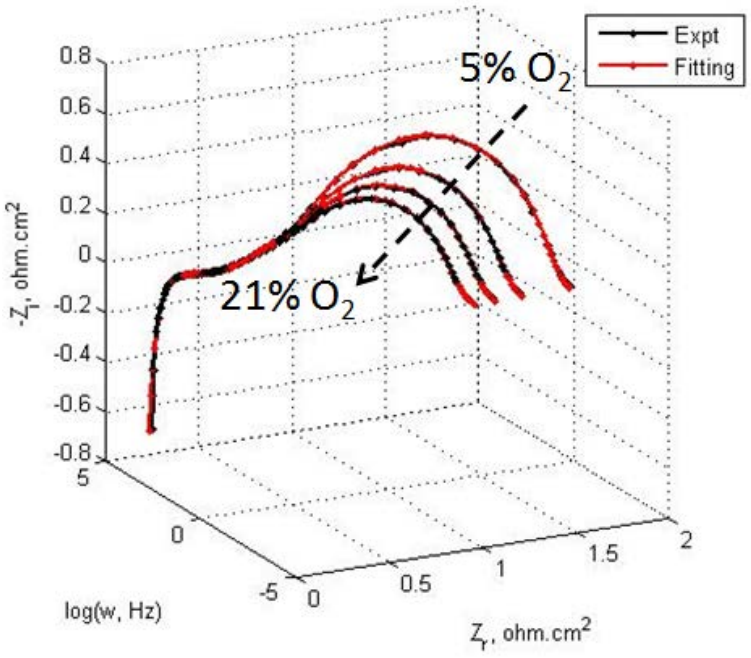

**Figure 3-6 Validation of frequency dependence of the proposed cathode model, when each curve at different $pO_2$ are fitted separately using the equivalent circuit proposed for the symmetric cathode cells (Figure 3-5).**

**Table 3-1 Fitted parameters for Figure 3-6 where oxygen partial pressure in cathode feeding stream varies from 21% to 2%**

| atm | $p(O_2)$ | 0.21 | 0.15 | 0.10 | 0.05 |
|---|---|---|---|---|---|
| $mol/cm^3$ | $prefactor = l_{TPB} \cdot C_{\max}$ | 0.359 | 0.317 | 0.315 | 0.325 |
| $cm^2/s$ | Ds | 6.88E-10 | 6.78E-10 | 6.73E-10 | 6.66E-10 |
| $ohm.cm^2$ | $R_F$ | 0.0137 | 0.0138 | 0.0137 | 0.0137 |
| $F/cm^2$ | $C_F$ | 0.188 | 0.172 | 0.154 | 0.133 |
| 1/Pa | K | 1.91E-4 | 6.05E-5 | 7.96E-5 | 4.73E-4 |
| 1/s | $k_{ads}$ | 0.274 | 0.506 | 0.470 | 0.221 |

With the inductance, the total ohmic resistance is a little bit smaller than what is read from the x-axis intercept. And the inductance and ohmic resistance stay almost the same in the wide range of $O_2$ we fitted. Therefore, their values are fixed by the average of the fitting results to further reduce the number of fitting parameters. This makes us to have totally 6 free fitting parameters, among which the prefactor is defined as $prefactor = l_{TPB} \cdot C_{\max}$ with $C_{\max}$ to be the maximum adsorbed surface species concentration per surface area. As can been seen in Table 3-1, the separate fitting of four curves at different $pO_2$ give almost consistent values for $D_s$, K and $k_{ads}$, which all should be material properties. The prefactor, which depends on microstructure of the porous electrode is also almost constant, which further confirms the goodness of the model. More importantly, Figure 3-6 shows the fitting not only gives a good match between real and imaginary part of the Nyquit plot, it also captures well the frequency dependence of each curve.

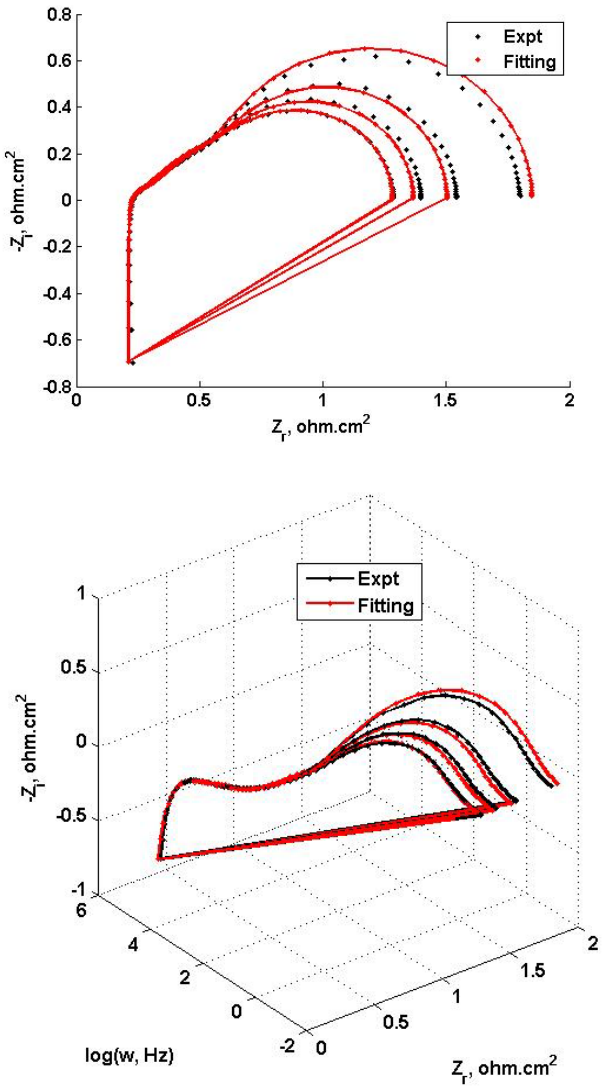


**Figure 3-7 Validation of $pO_2$ dependence of the proposed cathode model, when all four curves at different $pO_2$ are fitted together with fixed material property parameters using the equivalent circuit proposed for the symmetric cathode cell. (Upper) 2D Nyquit plot. (Bottom) 3D plot showing frequency dependence.**

Since the fitted material property and microstructure related parameters do not change too much with $pO_2$, their average values are taken to further reduce the number of fitting parameters when all four curves in Figure 3-6 are fitted together. In this case, only high frequency resistance $R_F$ and capacitance $C_F$ are fitted. As can be seen in Figure 3-7, fitting results confirms that the model can well capture the $pO_2$ dependence as well, only showing slight deviation for 5% and 10% $pO_2$ impedance curves.

### 3.5.2 Microstructure of the cathode functional layer (CFL)

In order to study the microstructure and performance relationship, we designed three sets of Saint-Gobain full cells using CFLs composed of different YSZ particles. With different YSZ particles, the microstructure (porosity, TPB density, length for surface adsorption) changes, and therefore it can help elucidate some effects of microstructure of porous electrode, and further help improve the CFL performance.

For fine, medium and coarse YSZ cells, the porosity values are 11%, 15% and 19% accordingly. SEM images were taken for these three samples and we can roughly estimate the number of TPB points on the SEM images. Assuming the TPB points density on the typical SEM image is representative for all depth of the CFL, and considering the tortuous pathways of the pores and the connected particles, we can estimate the TPB density in the unit of length per electrode area by using number of TPB sites per electrode area times CFL thickness, and times CFL tortuosity (Equation 3-14).

**Equation 3-14** $TPB\ density\ \left(length / \text{electrode}\, area\right) = TPB\ sites\ per\ area \cdot \mathrm{L}_{CFL} \cdot \tau_{\mathrm{P\_CFL}}$

For the surface diffusion length $L_s$, we can estimate it from measuring the distance from along the LSM particles between any two TPB points, and divide it by two. All possible LSM surface paths are measured and average or medium values for $L_s$ are estimated. Table 3-2 shows the experimentally measured porosity and manually estimated TPB point density and average surface diffusion length $L_s$ from their SEM images respectively.

The impedance curves were measured at OCV for these three different cells with different YSZ particles.

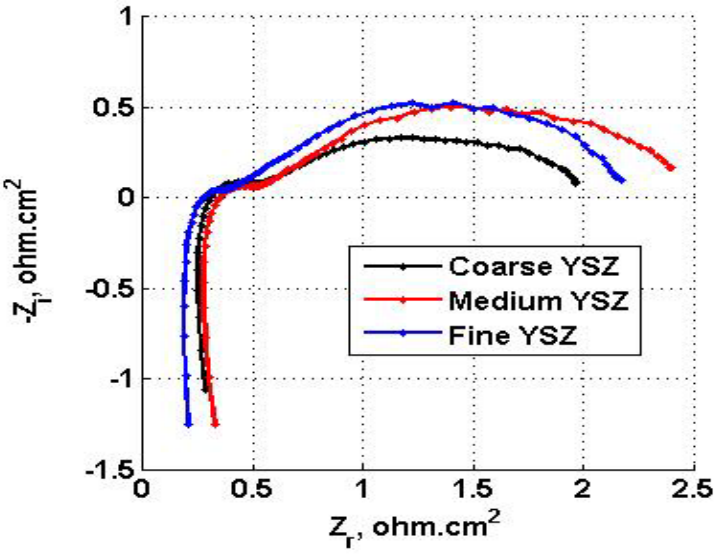


**Figure 3-8 Impedance measured at open circuit for three Saint-Gobain full cells that use coarse, medium and fine YSZ particles for the cathode functional layers, respectively.**

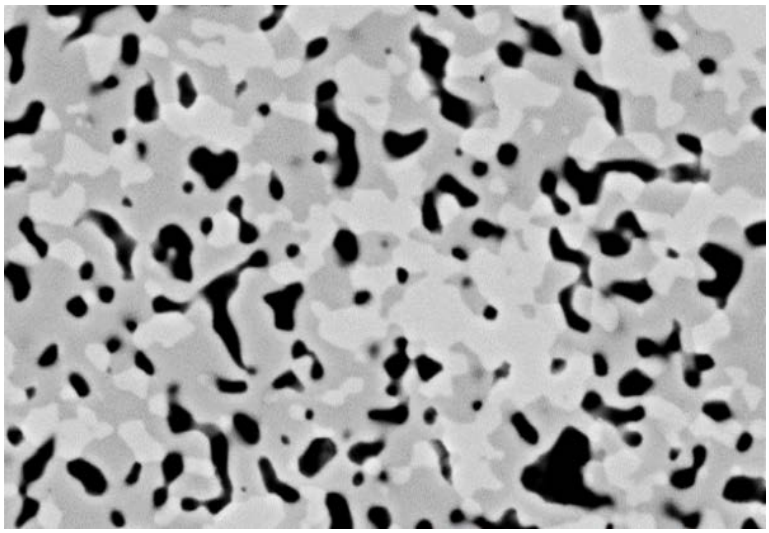

**Figure 3-9 Typical SEM images of Saint-Gobain cells when fine, medium and coarse YSZ particles are used in cathode functional layers. (Dark grey–YSZ, light gray–LSM, black–Pore) Note: for confidential reasons, only one image was shown, and scale bar is not included.**

From the derived analytical impedance (Equation 3-13) of the cathode adsorption-diffusion process, we see that the higher TPB density would lead to lower impedance. However, as shown in Figure 3-8, to our surprise, the cell performance boosts with coarse

YSZ particles, and cell with medium YSZ particles have the largest resistance. This is hard to be explained by only considering the difference in TPB densities among three cells. First we wondered if the gas phase transport in CFL could be a big resistance source. We estimated the gas diffusion resistance using Equation 2-15 and found that even if the pore size of the cathode functional layer is as small as 0.5um, the gas diffusion resistance resulting from the CFL is still less than 2% of that of the anode side, therefore, it is unlikely for the gas diffusion to be the main cause for different responses for these three different cells.

**Table 3-2 The experimentally measured porosity and manually estimated TPB point density and average surface diffusion length from their SEM images**

| YSZ particles | Porosity | Number of TPB per electrode area ($1/um^2$) | Average $L_s$ (um) |
|---|---|---|---|
| **Fine** | 0.11 | 0.235 | 0.614 |
| **Medium** | 0.15 | 0.438 | 0.430 |
| **Coarse** | 0.19 | 0.261 | 0.968 |

Then there are two possible reasons, 1) TPB density estimated from the SEM images include all TPB sites, however, due to the connectivity issues and percolation effects for different phases (LSM, YSZ and pore phases), it is possible that part of the TPB sites are actually not electrochemically active and should not be counted into the effective TPB density when one studies the relationship between microstructure of the porous electrode and cell performance. Or it is also possible that 2) TPB density may not be the main microstructure factor that affect the cell performance. As we can see in the analytical expression, there are other important microstructure parameters, for example, surface diffusion length $L_s$ , which could also be influential in terms of determining the impedance values.

For the former arguments, there are several papers theoretically studied the TPB density using geometry-based models. Some papers mentioned that there is a certain optimal composition for the LSM/YSZ composite electrode, for which the cell performance can be optimized. Also, the particle sizes of the YSZ and LSM, and especially ratio of these

two types of particles is also a vital factor. One typical study was conducted by Gokhale in 2009[87], who derived an analytical equation for total triple phase boundary length per unit volume in an isotropic uniform random microstructure of LSM/YSZ composite cathode. The equation is applicable to YSZ and LSM particles of any convex shapes and size distributions, and it explicitly relates TPB density to the shapes, mean sizes, coefficient of variation (a measure of the spread in a size distribution) and skewness of YSZ and LSM particle populations, and volume fractions of YSZ, LSM, and porosity. Their parametric analysis reveals that (1) non-equiaxed plate-like, flake-like, and needle-like YSZ and LSM particle shapes can yield substantially higher TPB density; (2) mono-sized YSZ and LSM powders lead to higher TPB density as compared to the powders having size distributions with large coefficient of variation; (3) TPB density is inversely proportional to the mean sizes of YSZ and LSM particles; and (4) high value of TPB density is obtained at the lowest porosity volume fraction that permits sufficient connectivity of the pores for gas permeability.

These are all very useful information for designing a better microstructure of the cathode functional layer. However, we have to note that this paper only considered the total TPB density. Due to the percolation effects, some TPB sites may not be well connected and therefore, what really matters is the electrochemically 'active' TPB density. In order to estimate the active TPB density, one has to include percolation theory for a composite porous media. In 2012, Gokhale[88] further incorporated the consideration of percolation, and studied topological connectivity of the triple phase boundaries in solid oxide fuel cell composite cathodes. Three-dimensional microstructure simulations are utilized to predict the topological connectivity of the triple phase boundaries in a composite SOFC cathode as a function of the volume fractions of the constituents, particle size, shape, and the thickness of the cathode. Several parameters have been studied for their effects on the activity on the TPB and the simulations showed that at a certain porosity volume fraction, the maximum TPB connectivity is achieved when the volume fractions of constituents are equal. The percolation threshold of porosity is about 5–10% and increasing porosity reduces TPB connectivity by compromising the connectivity of constituents. They summarized the results in a ternary contour plot of the fraction of the length of connected TPB in the length of total TPB (Figure 3-10). Since theoretical percolation study requires

stochastic modeling technique, which is not the author's expertise, this aspect is not studied in this thesis.

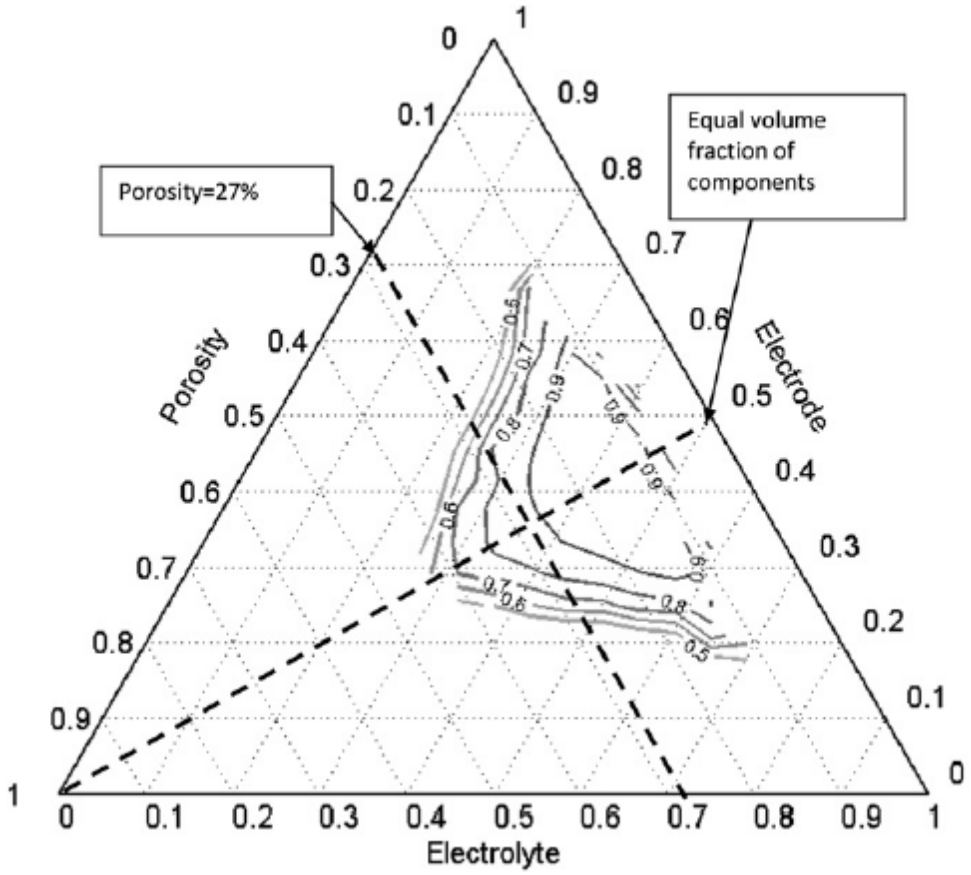


**Figure 3-10 Copy of the Figure.11 of Gokhale's paper in 2012[88]. Ternary contour plot of the fraction of the length of connected TPB in the length of total TPB. Spherical particles of the two components have the same radius. The thickness of the electrodes is 18 times the particle radius.**

As shown in Table 3-2, the estimated $L_s$ is the highest in the coarse YSZ cell, and relatively low in the fine and medium cells. This means it could be possible that the longer the $L_s$ , the smaller the resistance is, though this seems contradictory to our intuition. With this guess kept in mind, further analysis on the effect of the surface diffusion length $L_s$ is necessary.

The fabrication teams in Saint-Gobain further carefully fabricated four symmetric cathode cells, which are all the same except for the microstructure of the cathode

functional layers. The materials used and their loading are the same, and the only difference is the pore sizes and connectivity of the three different phases. SEM images were taken and then analyzed to estimate the TPB density and the diffusion length $L_s$ again. A software was utilized to count more accurately the number of TPB points and measure LSM/pore surface lengths. Then the no bias AC impedance curves were fitted and corresponding boundary layer thickness $l_\delta$ values were calculated based on the fitting results.

**Table 3-3 Estimated parameters, and fitted parameters for all four symmetric cathode cells. Boundary layer thickness values are calculated from fitted parameters and shown in the last row.**

| | Units | Cell A | Cell B | Cell C | Cell D |
|---|---|---|---|---|---|
| **Median $L_s$** | um | 0.29 | 0.41 | 0.31 | 0.20 |
| **#TPB/area** | $1/um^2$ | 0.23 | 0.32 | 0.33 | 0.32 |
| **$l_\delta$ at 21% $O_2$** | um | 0.30 | 0.29 | 0.22 | 0.36 |

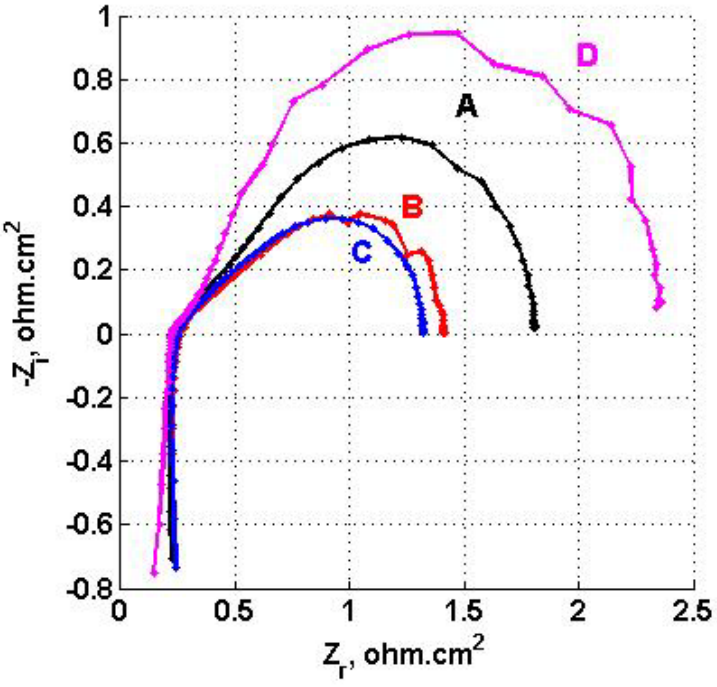


**Figure 3-11 No bias AC impedance measured at OCV, 800ºC and 21% pO2 for all four Saint-Gobain cells**

Figure 3-11 shows the impedance measured at OCV of these four cells, and Table 3-3 gives all the estimated parameters, and calculated boundary layer thickness $l_\delta$ according to the fitted parameters for all four symmetric cathode cells. Boundary layer thickness values ($l_\delta$) are calculated from the fitted parameters and shown in the last row. We can see that Cell D, which has the smallest $L_s$, gives the largest resistance; while cell B and C have much larger $L_s$, give similar and almost the smallest resistances. When we fitted the four impedance curves, we obtained the effective gas adsorption rate constant k and the surface diffusivity $D_s$, then the boundary layer thickness can be calculated for each cell. From comparison among the calculated $l_\delta$ and the surface diffusion length $L_s$, we found that the relativeness of these two length values is critical for determining the cell performance. Cell D not only has the smallest $L_s$, it also has the biggest $l_\delta$, which overall gives the highest resistance. In contrast, cell C has relatively big $L_s$, especially when compared to its $l_\delta$ values, therefore it gives the smallest resistance from the surface diffusion-gas adsorption process. Cell B and A are the cases in between. Actually, this is the exactly the same concept of Thiele modulus (Equation 3-15).

**Equation 3-15** $$\phi = \frac{L_s}{l_\delta} = \frac{L_s}{\sqrt{D_s / k}}$$

From this analysis we see that the relative reaction rate of surface diffusion and surface adsorption is a critical value which will determine the goodness of the catalyst. When the Thiele modulus is much larger than one (left panel of Figure 3-12), the catalyst surface is well covered by the adsorbed species, and the overall process is rate limited by the surface diffusion inside a very thin boundary layer. In this scenario, the catalyst shows good activity. While Thiele modulus is much smaller than one (right panel of Figure 3-12) the gas adsorption process is too slow so that it becomes rate determining. All the species adsorbed onto the surface will quickly diffuse to the reaction site, leaving the catalyst surface barely covered by the surface species. Therefore, in this case, the catalyst shows relatively bad activity.

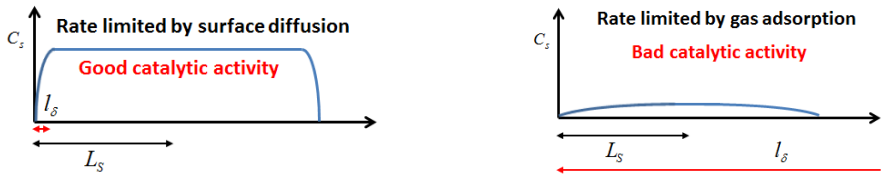


**Figure 3-12 Schematic to demonstrate the importance of the Thiele modulus in electrocatalysis. (Left) Thiele modulus is much larger than one (Right) Thiele modulus is much smaller than one.**

When plotting the theoretical impedance responses from the analytical impedance response (Figure 3-13), we can see that when the surface diffusion length $L_s$ is small, especially much smaller than the boundary layer thickness, the impedance response of the cathode surface process gives a semicircle followed by a small portion of the 45 degree line in high frequency regime. In this case, the oxygen gas species that adsorbed onto LSM quickly diffuses towards the TPB, and therefore, the surface concentration of oxygen intermediate on the LSM surface is low. Surface adsorption of the gas species is rate limiting, and the LSM particle shows bad catalytic activity. When the surface diffusion length $L_s$ increases, the semicircle became more and more depressed, with a larger portion of the 45 degree line. Then when the surface diffusion length $L_s$ further increase, especially when it is much larger than the boundary layer thickness $l_\delta$, the impedance of the cathode process has a shape similar to Warburg element, showing a 45 degree line in high frequency regime followed by a depressed semicircle. In this case, oxygen gas quickly adsorbed onto LSM surface (good catalytic activity), and the surface diffusion becomes relatively slow, and rate determining.

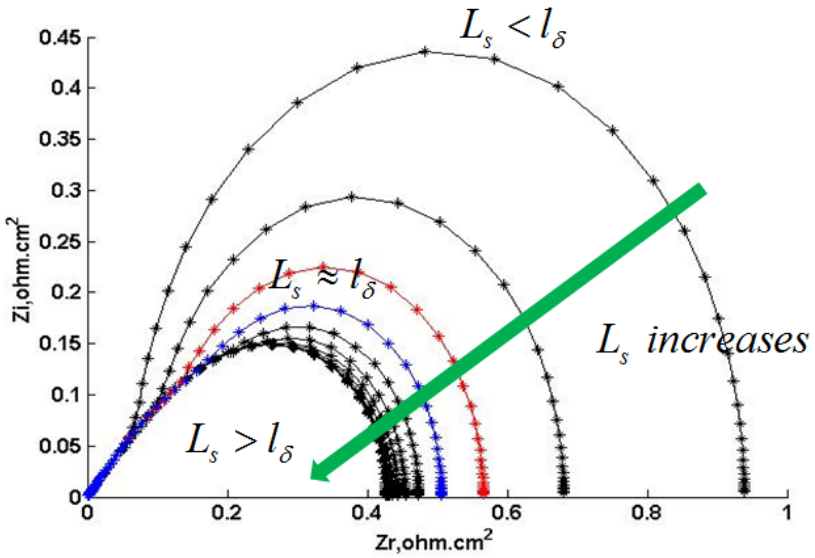


**Figure 3-13 Theoretical impedance response from cathode surface diffusion process when surface diffusion length $L_s$ is gradually changed. This plot uses a boundary length of 0.2043 um.**

From this analysis, we can see that the ratio of the surface diffusion length $L_s$ and the boundary layer thickness $l_\delta$ is critical, determining which process is more rate-limiting in the cathode surface process. When the low frequency resistance $R_G$ is plotted with respect to this ratio, it can be seen (Figure 3-14) that $R_G$ decreases sharply when the ratio increases. When the ratio is less than one, the resistance is relatively big, and the curve is steep; while when the ratio increases, the resistance gradually reaches a plateau. Four data points from the four Saint-Gobain cells were also added in the same plot, which can be seen that they are very close to the theoretical predicted curve. This plot shows well the competition between the surface diffusion and gas adsorption. Since these two processes are coupled together, and the rates are close to each other, the cathode surface model has to take both into consideration.

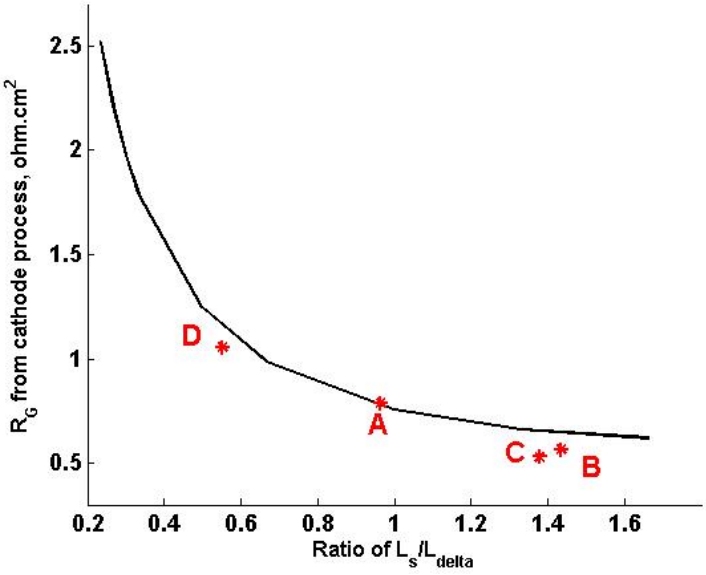


**Figure 3-14 The low frequency resistance $R_G$ dependence on the ratio of the surface diffusion length $L_s$ and the boundary layer thickness, at 800 ºC and 21% of $pO_2$.**

We also studied the theoretical effects of the thermodynamically equilibrium constant K and oxygen partial pressure $pO_2$ according to Equation 3-13. As can be seen in Figure 3-15 and Figure 3-16, both plots give a volcano shaped curve, which can actually described by the Sabatier principle, which is named after French chemist Paul Sabatier. It is a qualitative way to predict the activity of heterogeneous catalysts. The principle states that in order to have high catalytic activity, the interaction between reactants and catalysts should neither be too strong nor too weak. This principle also applies to electrocatalysis, where basically some adsorption is favored, but not too much. If the interaction is too weak, i.e., if $pO_2$ is too low or K is too small, there will be no reaction on the surface because it is difficult for catalyst surface to bind the reactants. If the interaction is too strong, i.e., if $pO_2$ is too high or K is too big, the surface sites are mostly occupied by surface intermediates, and there is not enough sites left for the transition state of the adsorption to stick at the surface, which will also lower the overall reaction rate. Sabatier principle usually gives rise to so-called volcano plot, such as examples shown in Figure 3-15 and Figure 3-16. The basic idea is that when plotting the rate of overall reaction on a heterogeneous catalyst with some adsorption property, for instance adsorption

equilibrium constant, according to Sabatier's principle the plot will have a maximum, showing the shape like a volcano. Being able to successfully produce the volcano plot predicted by the Sabatier principle also corroborate our analysis and the analytically derived impedance response (Equation 3-13).

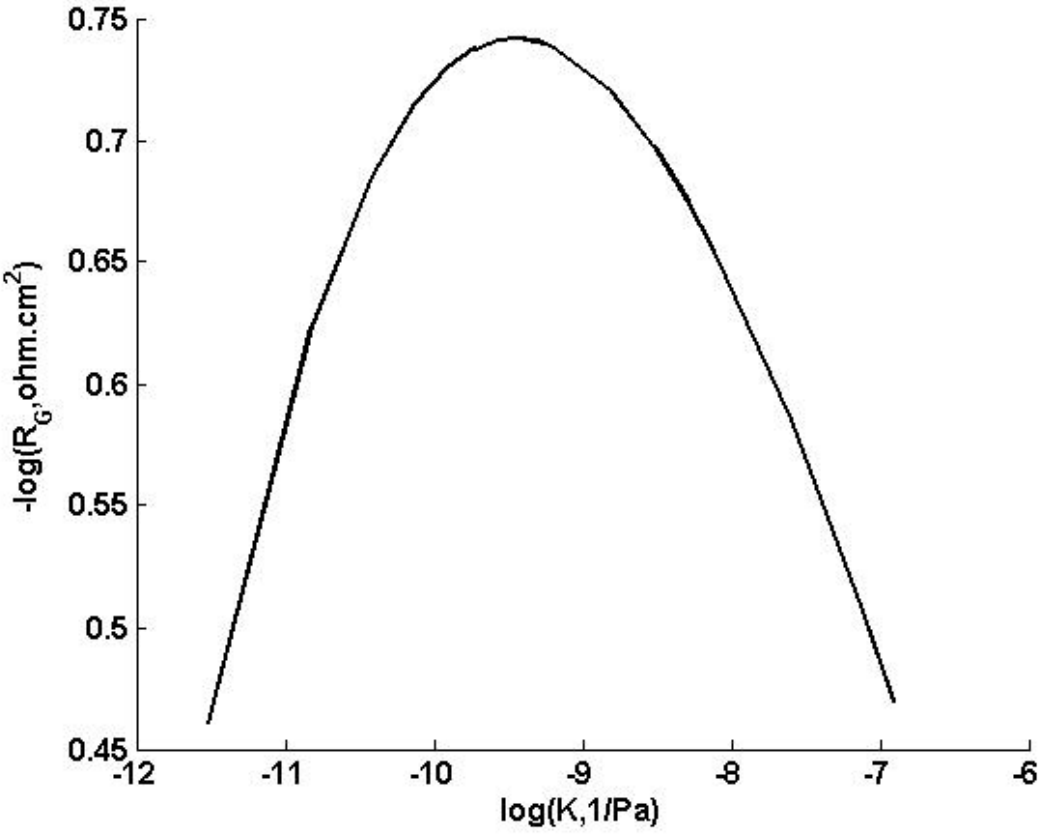


**Figure 3-15 The theoretical effect of the thermodynamically equilibrium constant K on the resistance of the cathode surface adsorption-diffusion process. The curve is plotted according to Equation 3-13.**

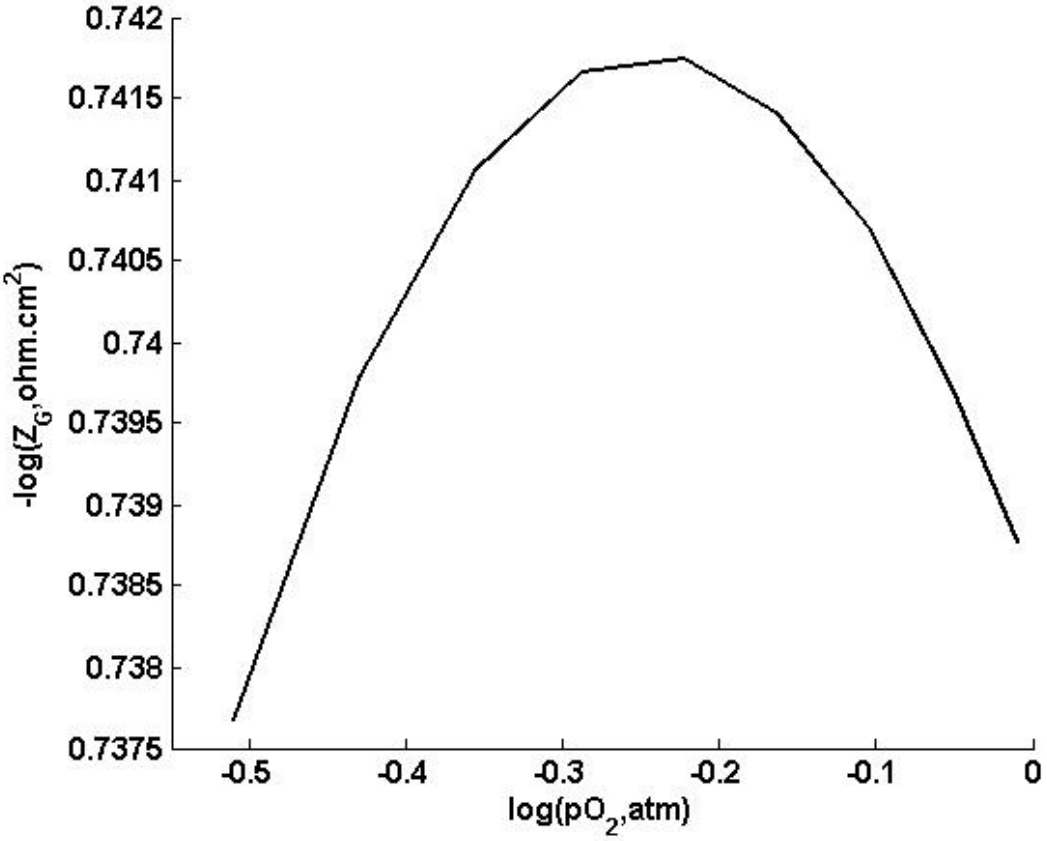


**Figure 3-16 The theoretical effect of the oxygen partial pressure $pO_2$ on the resistance of the cathode surface adsorption-diffusion process. The curve is plotted according to Equation 3-13.**

## 3.6 Conclusion

In this chapter, we have developed a theoretical model for the cathode electrocatalysis process, where a governing equation with both surface diffusion and surface adsorption with the Langmuir kinetic expression was used. This model describes the coupled process of oxygen gas dissociative adsorption onto the LSM surface, and surface diffusion of the oxygen intermediate on LSM surface to the TPB sites. It is able to capture the frequency dependence and the oxygen partial pressure dependence of the symmetric cathode cells, which use the same cathode functional layer as Saint-Gobain full cell. The model was also used to correlate microstructure of the porous cathode functional layer to the impedance response, and was able to describe the relationship between the Thiele

modulus ($\phi = L_s / l_\delta$) and the impedance response. By comparing experimental data from four different cells with theoretical prediction of the proposed electrocatalysis model, it shows that Thiele modulus should not be too big or small. For a specific boundary layer thickness $l_\delta$, the CFL microstructure should be tuned to provide $L_s$ which is large enough for providing enough surface sites for adsorption, and also small enough to guarantee a relatively high TPB density for charge transfer. Moreover, being able to successfully produce the volcano plot predicted by the Sabatier Principle also corroborate our analysis and the analytically derived impedance response (Equation 3-13).

## 3.7 Appendix: Derivation of the Nernst equation and relationship between $\Delta V$ and $\Delta\theta$

1) Derivation of the Nernst equation

The electrochemical reaction occurring at the TPB is:

$$O_{(ad)} + 2e^-_{(LSM)} \leftrightarrow O^{-2}_{(YSZ)}$$

At equilibrium we can write:

$$\mu_O + 2\mu_{e^-} = \mu_{O^{-2}}$$

With $\mu_O = \mu_O^\Theta + kT \ln a_O$ and $a_O = \dfrac{\theta}{1-\theta}$ as it is a species in a lattice.

$\mu_{e^-} = \mu_{e^-}^\Theta + kT \ln a_e - e\phi_{LSM}$ and we can assume $a_{e^-} = 1$

$\mu_{O^{-2}} = \mu_{O^{-2}}^\Theta + kT \ln a_{O^{-2}} - 2e\phi_{YSZ}$ and we can assume $a_{O^{-2}} = 1$

So we can derive the Nernst equation for the reaction at TPB.

$$\mu_O^\Theta + kT \ln \frac{\theta}{1-\theta} + 2\mu_{e^-}^\Theta - 2e\phi_{LSM} = \mu_{O^{-2}}^\Theta - 2e\phi_{YSZ}$$

$$-\left(\mu_{O^{-2}}^\Theta - \mu_O^\Theta - 2\mu_{e^-}^\Theta\right) + kT \ln \frac{\theta}{1-\theta} = 2e\left(\phi_{LSM} - \phi_{YSZ}\right)$$

$$\phi_{LSM} - \phi_{YSZ} = -\frac{\left(\mu_{O^{-2}}^{\Theta} - \mu_{O}^{\Theta} - 2\mu_{e^-}^{\Theta}\right)}{2e} + \frac{kT}{2e}\ln\frac{\theta}{1-\theta}$$

$$V = V^{\Theta} + \frac{kT}{2e}\ln\frac{\theta}{1-\theta}$$

2) Relationship between $\Delta V$ and $\Delta\theta$

At equilibrium the Nernst equation is:

$$V^{eq} = V^{\Theta} + \frac{kT}{2e}\ln\frac{\theta^{eq}}{1-\theta^{eq}}$$

Then we can apply a perturbation of voltage $\Delta V$:

$$V = V^{\Theta} + \frac{kT}{2e}\ln\frac{\theta}{1-\theta} \qquad \text{with } V = V^{eq} + \Delta V \text{ and } \theta = \theta^{eq} + \Delta\theta$$

By subtracting the two last equations we get:

$$\Delta V = V - V^{eq} = \frac{kT}{2e}\ln\left(\frac{\theta}{1-\theta}\frac{1-\theta^{eq}}{\theta^{eq}}\right) = \frac{kT}{2e}\ln\left(\frac{\theta}{\theta^{eq}}\frac{1-\theta^{eq}}{1-\theta}\right)$$

Now we substitute $\theta = \theta^{eq} + \Delta\theta$:

$$\Delta V = \frac{kT}{2e}\ln\left(\frac{\theta^{eq} + \Delta\theta}{\theta^{eq}}\frac{1-\theta^{eq}}{1-\theta^{eq} - \Delta\theta}\right)$$

Then, just do some simple algebraic calculations, it will give us a relationship between voltage perturbation $\Delta V$ and the surface concentration perturbation $\Delta\theta$.

$$\Delta V = \frac{kT}{2e}\ln\left(\frac{\theta^{eq} + \Delta\theta}{\theta^{eq}}\right) - \frac{kT}{2e}\ln\left(\frac{1-\theta^{eq} - \Delta\theta}{1-\theta^{eq}}\right)$$

$$\Delta V = \frac{kT}{2e}\ln\left(1 + \frac{\Delta\theta}{\theta^{eq}}\right) - \frac{kT}{2e}\ln\left(1 - \frac{\Delta\theta}{1-\theta^{eq}}\right)$$

Since in impedance measurement, the perturbation is very small, and we can assume that $\Delta\theta << \theta^{eq}$ and $\Delta\theta << 1-\theta^{eq}$, therefore we can apply the Taylor expansion to the natural logarithms to get:

$$\Delta V = \frac{kT}{2e}\frac{\Delta\theta}{\theta^{eq}} + \frac{kT}{2e}\frac{\Delta\theta}{1-\theta^{eq}}$$

$$\Delta V = \frac{kT}{2e}\Delta\theta\left(\frac{1}{\theta^{eq}} + \frac{1}{1-\theta^{eq}}\right)$$

Finally, the derivation provides the relationship between $\Delta\theta$ and $\Delta V$. Note that at the denominator there is an additional $1-\theta^{eq}$ term, this is due to the fact that the Nernst equation involves $1-\theta$ too (that we can see as the activity of adsorbed oxygen in a lattice or as the contribution of surface vacancies).

# Chapter 4. Modeling of Saint-Gobain full cell

## 4.1 Introduction

The Saint-Gobain full cell composes anode, cathode and the electrolyte in between. In Chapter 2 and 3, we have identified the main resistance source of the anode and cathode to be anode gas diffusion in anode support layer and oxygen adsorption and surface diffusion in cathode functional layer, using anode-supported cell and symmetric cathode cell, respectively. Here we applied these understandings into a full cell model, using a proposed equivalent circuit model again. Knowing the main resistance makes it possible for us to propose a physics-based equivalent circuit which captures main physical processes, but is still as simple as possible so that not too many fitting parameters are present.

## 4.2 Full cell model development

We incorporated the cathode surface element we derived into an equivalent circuit for the Saint-Gobain full cell analysis (Figure 4-1). Again, Resistance R1 represents the total ohmic resistance of the SOFC button cell, mainly coming from the electrolyte ohmic resistance and other contact resistances. The R2 and C1 in parallel (called $R_F$ and $C_F$ in fitting results) accounts for the reactions associated with high frequency arc. It can come from both anode and cathode charge transfer reactions. The ideal finite length Warburg impedance accounts for the multicomponent gas diffusion for anode, where the effective diffusivity for hydrogen can be approximated by the following equation (Equation 4-1).

**Equation 4-1** $$Z_W = \left(\frac{RT}{n \cdot F}\right)^2 \frac{1}{D \cdot P_{H_2}} \frac{\tanh\left(\sqrt{\frac{i \cdot \omega}{D}} L\right)}{\sqrt{\frac{i \cdot \omega}{D}}}$$

Lastly, the Gerischer type element is associated with a finite length surface diffusion/adsorption process, whose impedance response was derived theoretically above (Equation 3-13).

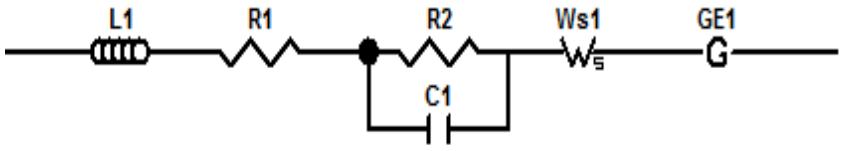


**Figure 4-1 Physics-based equivalent circuit model for the Saint-Gobain button cell.**

The symmetric cathode cells in chapter 3 use the same way of fabricating cathode functional layer as the Saint-Gobain full cell, therefore, the microstructure, composition and material properties of LSM should be close to each other in these two types of the cells. Since most of the fitting parameters (including $k_{ads}$, K, $D_s$ and D) are material properties, and the prefactor is microstructure related, they should not vary too much when operating conditions of gas composition is changed. Therefore, we took average values of them from fitting of the symmetric cathode cells and used them as fixed values when fitting for the full Saint-Gobain cell.

## 4.3 Fitting results of full Saint-Gobain cell

The fitted impedance curves are shown in Figure 4-2. When we adopted the average values of the fitted material properties and microstructure related parameters from the study of symmetric cathode cell, the Saint-Gobain cell's impedance fitting go very well again for a wide range of oxygen partial pressure (Figure 4-2). When we plot impedance response of each process (inductance, high frequency charge transfer reaction, anode Warburg gas diffusion, cathode Gerischer type surface adsorption/diffusion) separately, their individual contribution and peak frequency can be clearly seen (Figure 4-3 and Figure 4-4). The inductance gives a fourth quadrant vertical line at the highest frequency regime; the RC in parallel gives a small arc in the high frequency regime; The Warburg

and Gerischer type impedance both give a semicircle followed by a 45 degree line, however their response are highly overlapped in the low to medium frequency region. It is also interesting to note that in Saint-Gobain's cell, the slowest process is not anode gas diffusion (with a peak frequency of around 8 Hz), instead, the oxygen adsorption and surface diffusion proceeds much slower (with a peak frequency locates at 0.5 Hz). And it is also the rate-limiting step that should be further studied in order to improve Saint-Gobain cell's overall performance.

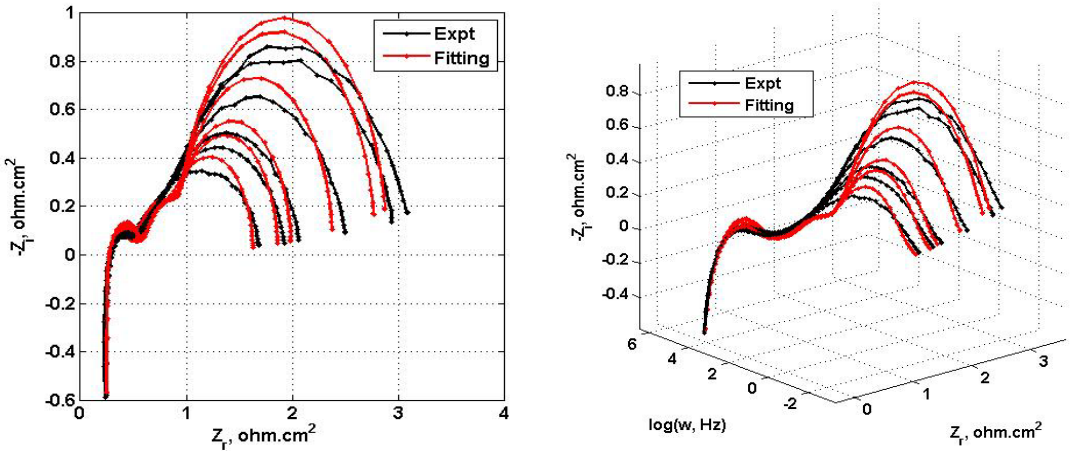


**Figure 4-2 Fitting results for Saint-Gobain cell when oxygen partial pressure $pO_2$ is varied ($pO_2$ is 2%, 3%, 5%, 10%, 15% and 21% for impedance curves with larger to smaller low frequency arcs). (Left) Nyquist plot showing relationship between imaginary part and real part (Right) 3D plot showing frequency dependence (in logarithmic scale) as well.**

## 4.4 Identification of rate limiting step in Saint-Gobain cell

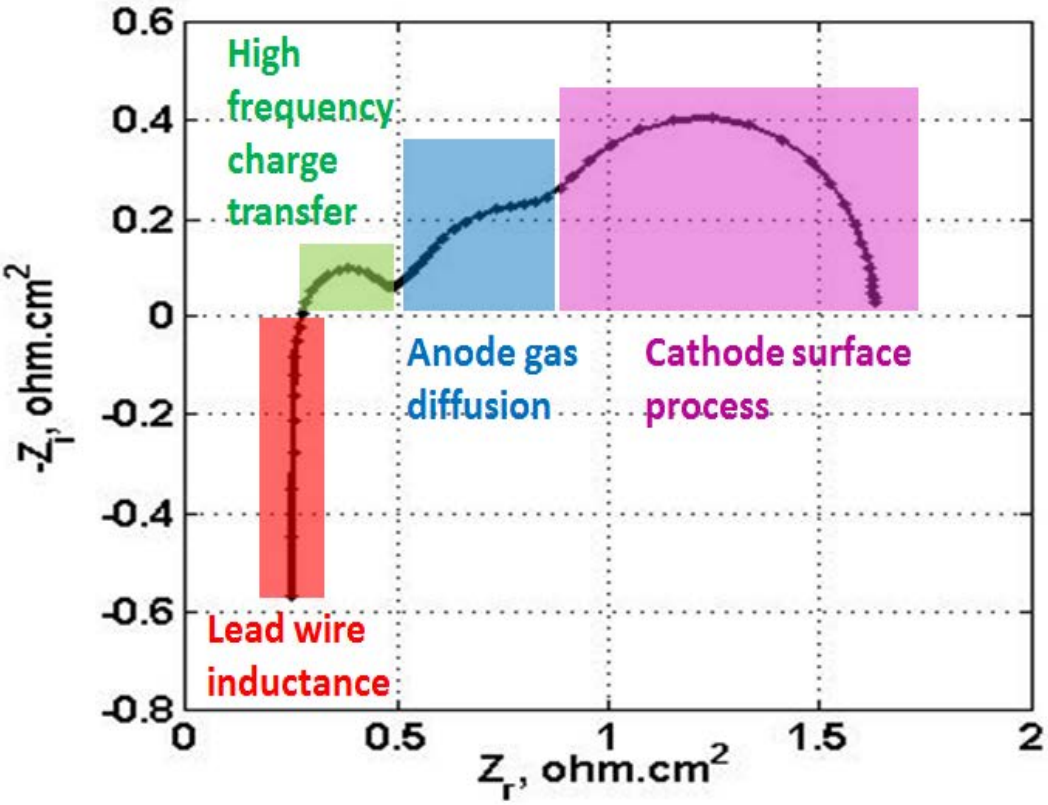


**Figure 4-3 Physical interpretation of the Saint-Gobain cell impedance data, showing different parts of the impedance responses in the fitted results for 21% $pO_2$ curve.**

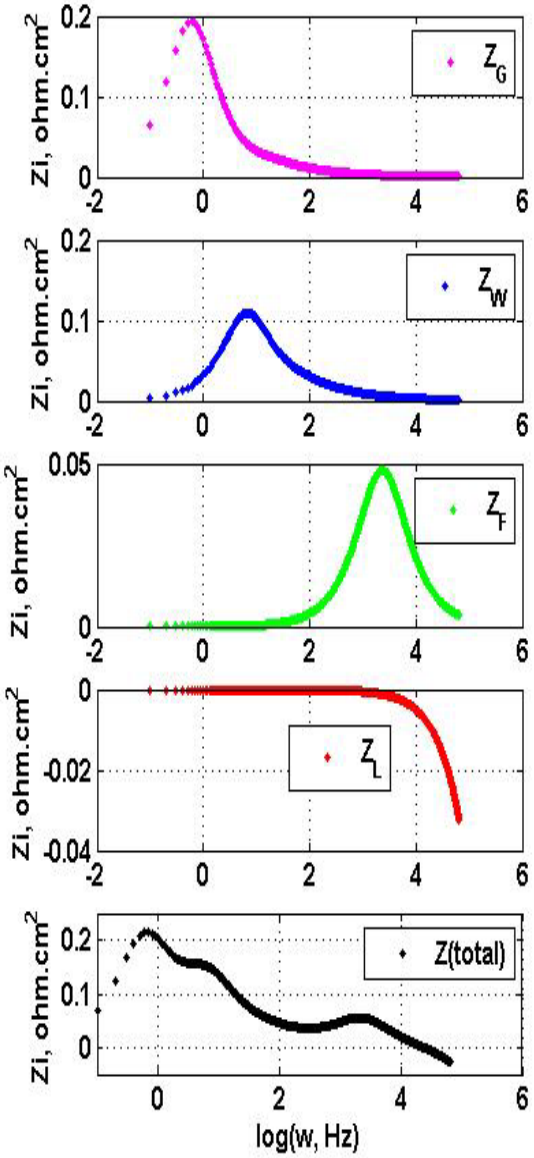


**Figure 4-4 Physical interpretation of the Saint-Gobain cell impedance data, showing different parts of the impedance responses in the fitted results for 21% $pO_2$ curve. $Z_G$ is the Gerischer response, $Z_W$ is the Warburg response, $Z_F$ is the RC circuit response, $Z_L$ is the inductance response. The combination of them plus the ohmic resistance are the total impedance response shown in the last row**.

Under the conditions we carried out the experiments, anode is always fed with 100% hydrogen while oxygen in cathode is varied from 21% to 2%, therefore the contribution from anode gas diffusion should not change while contribution from cathode process co-

limited by gas adsorption and surface diffusion should vary accordingly. The fitting results show exactly the same trend as predicted. The Warburg response is almost the same when $O_2$ partial pressure is changed, while the Gerischer type response increases a lot when $O_2$ partial pressure decreases from 21% to 2%. And the increase of Gerischer type response covers most of the total impedance increase. This consistency again ensures the goodness of the proposed equivalent circuit and the goodness of fitting.

## 4.5 Conclusion

Based on the understanding we achieved from chapter 2 and 3, a physics-based equivalent circuit model was proposed, and impedance of Saint-Gobain cells can be fitted well accordingly. Fitting gives reasonable reaction rate constant, adsorption equilibrium constant, effective gas diffusivities and oxygen surface diffusivities again. Moreover, the contributions from anode gas diffusion and cathode adsorption/diffusion resistance is consistent with our expectation based on the operating conditions. This analysis also tells us the slowest process in Saint-Gobain cells is not gas diffusion, instead, a process co-limited by oxygen adsorption and surface adsorption at the cathode functional layer is the main source of the big low frequency arc. This interpretation of the full impedance data would greatly help to better understand the cells, and would facilitate the performance improvement of the Saint-Gobain cell.

# Chapter 5. Conclusions and Recommendations for future work

## 5.1 Conclusions

This PhD research work addressed two important aspects of the numerical modeling of SOFCs: the multicomponent gas diffusion in porous electrode at the anode and the heterogeneous electrocatalysis of oxygen reduction reaction (ORR) at the cathode.

We developed a theoretical framework to analyze gas diffusion resistance $R_b$ for AC impedance spectra of commercial Julich cell (anode-supported solid oxide fuel cell). Instead of invoking high tortuosity values to explain the limiting current in current-voltage curves, the tortuosity fitted from impedance measurements using the Dusty Gas model is physically reasonable, and does not vary with gas pressure. This method can also be extended to analyze nonzero current impedance or impedance measured at different temperatures. Fitted tortuosity values are consistent with both direct physical measurements and theoretical predictions.

Our gas diffusion analysis shows gas diffusion resistance is only significant at anode side for both Julich cell and Saint-Gobain cell. Different from Julich cell, the impedance response in low to medium frequency arc also contains contributions from some other cathode processes in the Saint-Gobain cell. Therefore, an electrocatalysis model describing oxygen adsorption and surface diffusion co-limited process was developed, and corresponding theoretical impedance response was derived. This cathode model is able to capture the frequency dependence and the oxygen partial pressure dependence of the symmetric cathode cells, which use the same cathode functional layer as Saint-Gobain full cells. The model was also used to correlate microstructure of the porous cathode functional layer to the impedance response, and was able to describe the relationship between the Thiele modulus (the ratio of surface diffusion length $L_s$ and the boundary layer thickness $l_\delta$) and the impedance response. An understanding of the

effects of the gas adsorption equilibrium constant $K$ and partial pressure $pO_2$ was also achieved, which is consistent with Sabatier principle.

Based on the above understanding, a physics-based equivalent circuit model was proposed, and impedance of Saint-Gobain cells can be fitted well accordingly. Fitting gives reasonable reaction rate constant, adsorption equilibrium constant, effective gas diffusivities and oxygen surface diffusivities. Moreover, the distribution of anode gas diffusion and cathode adsorption/diffusion resistance is consistent with our expectation based on the operating conditions. This analysis also tells us the slowest process in Saint-Gobain cells is not gas diffusion, instead, an electrocatalytic process co-limited by oxygen adsorption and surface adsorption at the cathode functional layer is the main source of the big low frequency arc when oxygen partial pressure decreases.

Moreover, the analytical impedance response can be implemented in Saint-Gobain's impedance software when necessary, in order for their staffs to use as a routine tool in the daily analysis. It can also be applied to any full numerical simulation (for both button cells and SOFC stacks). Not only the IV curves, AC impedance could be simulated, any type of electrochemical responses, such as transient processes can be analyzed for further investigations. To our best knowledge, up to now, most numerical simulation works use Butler-Volmer type reaction kinetics for the cathode modeling, assuming charge transfer is the rate limiting step, and very few papers have adopted other types of rate determining kinetics. However, if the surface process is rate limiting as suggested by this research work, one should incorporate the governing equations of the cathode surface process into a PDE model for the full cell or stack for a more accurate numerical simulation.

To summarize, a better understanding of the anode gas diffusion process and the cathode electrocatalytic process achieved is critical for us (and the sponsor Saint-Gobain as well) in terms of qualitatively analyzing SOFC performance. To be more general, they can also be extended to other fields involving multi-component gas transport in porous media and electrocatalytic chemistry in energy converting cells.

From the engineering point of view, we have known that Saint-Gobain button cell could possibly limited by CFL, and anode bulk layer, anode functional layer and cathode bulk layer have their smaller resistances consecutively. At the same time, this specific

generation of SOFC button cells provided by Saint-Gobain should use slightly larger YSZ and LSM grains (to achieve Thiele modulus >> 1, but still maintain high enough TPB density) in cathode functional layer, and should also possibly use thicker cathode functional layer to provide higher TPB density per electrode area.

We also concluded that Dusty Gas model works better than Stefan-Maxwell and Fick's law, and should be implemented in full numerical simulation that Saint-Gobain may carry out. Though some commercial software packages do not have the Dusty Gas model module available, it should be added urgently in order for more accurate simulation of the complicated SOFC system, and in more general sense, of any system involves multicomponent gas diffusion through porous media.

## 5.2 Future work

### 5.2.1 CFL microstructure optimization

Since we have achieved a better understanding of the microstructure-performance relationship, more work can be carried out at the fabrication and testing side, in order to experimentally improve the cathode functional layer. By doing so, we expect the Saint-Gobain cell would be able to obtain another generation of button cells which have lower internal resistance and higher power density, compared to the one they provided for this research work.

### 5.2.2 Study on high current ORR mechanism

We have to admit that the cathode catalytic model developed here for the oxygen reduction reaction (ORR) is only for open circuit condition, and is not applicable to high current impedance analysis, especially when a large current is drawn from the operating cell. Therefore, more careful study needs to be carried out to investigate high current operating conditions and determine a current value at which the oxygen reduction reaction at cathode could switch to other mechanisms, such as bulk pathway. Only by doing that can we continue with the study of degradation issue of the SOFC, which may need to include consideration of ORR mechanism at high current.

### 5.2.3 Stack model

For the modeling work carried out in Saint-Gobain, the full numerical PDE model should adopt the surface diffusion-adsorption equations to describe the oxygen reduction reaction at the cathode functional layer, and should use the Dusty Gas Model for gas diffusion through porous anode bulk layer. This suggestions also applied to any other research work of SOFC modeling.

### 5.2.4 Flexible fuels

In reality, when SOFC is used in commercialized market, it has to be operated based on hydrocarbon fuels, which is a complicated mixture of different types of hydrocarbons, such as natural gas. In that case, steam reforming reaction will occur in the gas phase, and soot formation will also be an extra reaction that has to be taken into account. Therefore, the reaction mechanism and reaction kinetics could be much more complicated, and require further intense study.

In sum, the SOFC is a complicated area where multicomponent gas transport, gas phase reaction, heterogeneous catalytic reaction and charge transfer in electrochemistry are all involved and coupled together. In order for the SOFC to be better understood and engineered, much more research works need to be carried out, to investigate the mechanism of transport, reaction and catalytic electrochemistry.

# Author's Related Publications

Diffuse charge and Faradaic reactions in porous electrodes, P. M. Biesheuvel, Y. Fu, and M. Z. Bazant, Phys. Rev. E 83, 061507 (2011).

Electrochemistry and capacitive charging of porous electrodes in asymmetric multicomponent electrolytes, P. M. Biesheuvel, Y. Fu and M. Z. Bazant, Russian J. Electrochem. 48, No. 6, pp. 580-592 (2012).

Multicomponent gas diffusion in porous electrodes, Y. FU, Y. Jiang, A. Dutta, A. Mohanram, J. D. Pietras, M. Z. Bazant, in preparation

Heterogeneous electrocatalysis in porous cathode of solid oxide fuel cells, Y. FU, S. Poizeau , A. Bertei, A. Dutta, A. Mohanram, J. D. Pietras, M. Z. Bazant, in preparation

Numerical modeling of solid oxide fuel cells with a heterogeneous electrocatalysis model, A. Bertei, Y. FU, M. Z. Bazant, in preparation

# Bibliography


(1) Http://babblogue.wordpress.com/tag/chemistry/.

(2) J. Bard, L. R. F. *Electrochemical Methods—Fundamentals and Applications*; John Wiley & Sons: New York, 2001.

(3) Macdonald, J. R. *Impedance Spectroscopy—Theory Experiment and Application*; John Wiley: New York, 2005; Vol. 144.

(4) E. Ivers-Tiffe´e, A. Weber, H. Schichlein, in: W. Vielstich, A.Lamm, A. G. (Eds. . *Handbook of Fuel Cells—fundamentals, Technology and Applications*; John Wiley & Sons: Chichester, 2003.

(5) S.C. Singhal, K. K. *High-Temperature Solid Oxide Fuel Cells:fundamentals, Design and Applications*; Elsevier Science: Oxford, 2003.

(6) M.J. Jùrgensen, S. Primdahl, M. M. Characterisation of Composite SOFC Cathodes Using Electrochemical Impedance Spectroscopy. *Electrochim. Acta* **1999**, *44*, 4195–4201.

(7) Mogensen, S. P. and M. Oxidation of Hydrogen on Ni / Yttria-Stabilized Zirconia Cermet Anodes. *Electrochem. Soc.* **1997**, *144*.

(8) H. Schichlein, A.C. Mu¨ller, M. Voigts, A. K. and E. I.-Ti. Deconvolution of Electrochemical Impedance Spectra for the Identification of Electrode Reaction Mechanisms in Solid Oxide Fuel Cells. *J. Appl. Electrochem* **2002**, *32*, 875–882.

(9) Bieberle, A.; Gauckler, L. J. Reaction Mechanism of Ni Pattern Anodes for Solid Oxide Fuel Cells. *Solid State Ionics* **2000**, *135*, 337–345.

(10) Jamnik, J.; Maier, J. Treatment of the Impedance of Mixed Conductors Equivalent Circuit Model and Explicit Approximate Solutions. *J. Electrochem. Soc* **1999**, *146*, 4183–4188.

(11) MacDonald, J. R. *Impedance Spectroscopy. Emphasizing Solid Materials and Systems*; John Wiley & Sons: New York, 1987.

(12) Mitterdorfer, A.; Gauckler, L. J. Identification of the Reaction Mechanism of the Pt,O2(g)|yttria-Stabilized Zirconia System Part II : Model Implementation , Parameter Estimation , and Validation. *Solid State Ionics* **1999**, *117*, 203–217.

(13) Mitterdorfer, A.; Gauckler, L. J. Identification of the Reaction Mechanism of the Pt , O 2 ( G ) U Yttria- Stabilized Zirconia System Part I : General Framework , Modelling , and Structural Investigation. *Solid State Ionics* **1999**, *117*, 187–202.

(14) E.Ahlberg, H. A. E. Ahlberg,1993.pdf. *Acta Chem. Scand.* **1993**, *47*, 1162.

(15) García-Camprubí, M.; Fueyo, N. Mass Transfer in Hydrogen-Fed Anode-Supported SOFCs. *Int. J. Hydrogen Energy* **2010**, *35*, 11551–11560.

(16) García-Camprubí, M.; Sánchez-Insa, a.; Fueyo, N. Multimodal Mass Transfer in Solid-Oxide Fuel-Cells. *Chem. Eng. Sci.* **2010**, *65*, 1668–1677.

(17) Suwanwarangkul, R.; Croiset, E.; Fowler, M. W.; Douglas, P. L.; Entchev, E.; Douglas, M. a. Performance Comparison of Fick's, Dusty-Gas and Stefan–Maxwell Models to Predict the Concentration Overpotential of a SOFC Anode. *J. Power Sources* **2003**, *122*, 9–18.

(18) Arpino, F.; Massarotti, N. Numerical Simulation of Mass and Energy Transport Phenomena in Solid Oxide Fuel Cells. *Energy* **2009**, *34*, 2033–2041.

(19) Hajimolana, S. A.; Hussain, M. A.; Daud, W. M. A. W.; Soroush, M.; Shamiri, a. Mathematical Modeling of Solid Oxide Fuel Cells: A Review. *Renew. Sustain. Energy Rev.* **2011**, *15*, 1893–1917.

(20) Bove, R.; Ubertini, S. Modeling Solid Oxide Fuel Cell Operation: Approaches, Techniques and Results. *J. Power Sources* **2006**, *159*, 543–559.

(21) Vural, Y.; Ma, L.; Ingham, D. B.; Pourkashanian, M. Comparison of the Multicomponent Mass Transfer Models for the Prediction of the Concentration Overpotential for Solid Oxide Fuel Cell Anodes. *J. Power Sources* **2010**, *195*, 4893–4904.

(22) J.W.Veldsink, R.M.J. van Damme, G.F. Versteeg, W. P. M. van S. The Use of the Dusty-Gas Model for the Description of Mass Transport with Chemical Reaction in Porous Media. *Chem. Engienering J.* **1995**, *57*, 115–125.

(23) Kookos, I. K. On the Diffusion in Porous Electrodes of SOFCs. *Chem. Eng. Sci.* **2012**, *69*, 571–577.

(24) Tsai, C.-L.; Schmidt, V. H. Tortuosity in Anode-Supported Proton Conductive Solid Oxide Fuel Cell Found from Current Flow Rates and Dusty-Gas Model. *J. Power Sources* **2011**, *196*, 692–699.

(25) Schmidt, V. H.; Tsai, C.-L. Anode-Pore Tortuosity in Solid Oxide Fuel Cells Found from Gas and Current Flow Rates. *J. Power Sources* **2008**, *180*, 253–264.

(26) Kim, J.; Virkar, A. V; Fung, K.; Mehta, K.; Singhal, S. C. Polarization Effects in Intermediate Temperature , Anode-Supported Solid Oxide Fuel Cells. **1999**, *146*, 69–78.

(27) Yoon, K. J.; Gopalan, S.; Pal, U. B. Analysis of Electrochemical Performance of SOFCs Using Polarization Modeling and Impedance Measurements. *J. Electrochem. Soc.* **2009**, *156*, B311.

(28) Zhu, H.; Kee, R. J. Modeling Electrochemical Impedance Spectra in SOFC Button Cells with Internal Methane Reforming. *J. Electrochem. Soc.* **2006**, *153*, A1765.

(29) Jiang, Y.; Virkar, A. V. Fuel Composition and Diluent Effect on Gas Transport and Performance of Anode-Supported SOFCs. *J. Electrochem. Soc.* **2003**, *150*, A942.

(30) Wilson, J. R.; Kobsiriphat, W.; Mendoza, R.; Chen, H.-Y.; Hiller, J. M.; Miller, D. J.; Thornton, K.; Voorhees, P. W.; Adler, S. B.; Barnett, S. a. Three-Dimensional Reconstruction of a Solid-Oxide Fuel-Cell Anode. *Nat. Mater.* **2006**, *5*, 541–544.

(31) Drescher, I.; Lehnert, W.; Meusinger, J.; Ju, D.-. Structural Properties of SOFC Anodes and Reactivity. **1998**, *43*.

(32) Izzo, J. R.; Joshi, A. S.; Grew, K. N.; Chiu, W. K. S.; Tkachuk, A.; Wang, S. H.; Yun, W. Nondestructive Reconstruction and Analysis of SOFC Anodes Using X-Ray Computed Tomography at Sub-50 Nm Resolution. *J. Electrochem. Soc.* **2008**, *155*, B504.

(33) Williford, R. E.; Chick, L. a.; Maupin, G. D.; Simner, S. P.; Stevenson, J. W. Diffusion Limitations in the Porous Anodes of SOFCs. *J. Electrochem. Soc.* **2003**, *150*, A1067.

(34) Ferguson, T. R.; Bazant, M. Z. Nonequilibrium Thermodynamics of Porous Electrodes. *J. Electrochem. Soc.* **2012**, *159*, A1967–A1985.

(35) Chick, L. a.; Meinhardt, K. D.; Simner, S. P.; Kirby, B. W.; Powell, M. R.; Canfield, N. L. Factors Affecting Limiting Current in Solid Oxide Fuel Cells or Debunking the Myth of Anode Diffusion Polarization. *J. Power Sources* **2011**, *196*, 4475–4482.

(36) Farhad, S.; Hamdullahpur, F. Micro-Modeling of Porous Composite Anodes for Solid Oxide Fuel Cells. *AIChE J.* **2012**, *58*, 1893–1906.

(37) Grew, K. N.; Chiu, W. K. S. A Review of Modeling and Simulation Techniques across the Length Scales for the Solid Oxide Fuel Cell. *J. Power Sources* **2012**, *199*, 1–13.

(38) Tseronis, K.; Kookos, I. K.; Theodoropoulos, C. Modelling Mass Transport in Solid Oxide Fuel Cell Anodes: A Case for a Multidimensional Dusty Gas-Based Model. *Chem. Eng. Sci.* **2008**, *63*, 5626–5638.

(39) Cayan, F. N.; Pakalapati, S. R.; Elizalde-Blancas, F.; Celik, I. On Modeling Multi-Component Diffusion inside the Porous Anode of Solid Oxide Fuel Cells Using Fick's Model. *J. Power Sources* **2009**, *192*, 467–474.

(40) Newman, J. Stefan–Maxwell Mass Transport. *Chem. Eng. Sci.* **2009**, *64*, 4796–4803.

(41) Runstedtler, A. On the Modified Stefan–Maxwell Equation for Isothermal Multicomponent Gaseous Diffusion. *Chem. Eng. Sci.* **2006**, *61*, 5021–5029.

(42) Krishna, R.; Wesselingh, J. A. The Maxwell-Stefan Approach to Mass Transfer. *Chem. Eng. Sci.* **1997**, *52*, 861–911.

(43) J.W.Veldsink, R.M.J. van Damme, G.F. Versteeg, W. P. M. van S. *Chem. Engienering J.* **1995**, *57*, 115–125.

(44) E.L. Cussler. Cussler, E. L. *Diffusion: mass transfer in fluid systems*, New York : Cambridge University Press, ***1997***

(45) Aris, J. P. G. K. and R. Communications on the Theory of Diffusion and Reactions-IX. Internal Pressure and Forced Flow for Reactions with Volume Change. *Chem. Eng. Sci.* **1973**, *28*, 2094–2098.

(46) R.Jackson, and R. H. H. Pressure Gradients in Porous Catalyst Pellets in the Intermediate Diffusion Regime. *Chem. Eng. Sci.* **1977**, *32*, 703–709.

(47) Davis, M. E.; Fairweather, G.; Yamanis, J. Analysis of SO2 Oxidation in Non-Isothermal Catalyst Pellets Using Dusty Gas Model. *Chem. Eng. Sci.* **1982**, *37*, 447–452.

(48) Bliek, A.; Van Poelje, W. M.; Van Swaaij, W. P. M.; Van Beckum, F. P. H. Effects of Intraparticle Heat and Mass Transfer during Devolatilization of a Single Coal Particle. *AIChE J.* **1985**, *31*, 1666–1681.

(49) Haberman, B. a.; Young, J. B. Diffusion and Chemical Reaction in the Porous Structures of Solid Oxide Fuel Cells. *J. Fuel Cell Sci. Technol.* **2006**, *3*, 312.

(50) Steele, B. C. H. Survey of Materials Selection for Ceramic Fuel Cells, II. Cathodes and Anodes. *Solid State Ionics* **1996**, *88*, 1223–1234.

(51) Mcevoy, A. J. Thin SOFC Electrolytes and Their Interfaces – A near-Term Research Strategy. **2000**, *132*, 159–165.

(52) Diethelm, S.; Closset, A.; Van, J.; Mcevoy, A. J.; Nisancioglu, K. Study of Oxygen Exchange and Transport in Mixed Conducting Cobaltates by Electrochemical Impedance Spectroscopy. *Solid State Ionics* **2000**, *135*, 613–618.

(53) Bredesen, R.; Mertins, F.; Norby, T. Measurements of Surface Exchange Kinetics and Chemical Diffusion in Dense Oxygen Selective Membranes. *Catal. Today* **2000**, *56*, 315–324.

(54) Lane, J. A.; Kilner, J. A. Measuring Oxygen Diffusion and Oxygen Surface Exchange by Conductivity Relaxation. **2000**, *137*, 997–1001.

(55) Lankhorst, M. H. R.; Bouwmeester, H. J. M.; Verweij, H. High-Temperature Coulometric Titration of $La_{1-x}Sr_xCoO_{3-Delta}$: Evidence for the Effect of Electronic Band Structure on Nonstoichiometry Behavior. **1997**, *567*, 555–567.

(56) Kim, S.; Yang, Y. L.; Jacobson, A. J.; Abeles, B. Diffusion and Surface Exchange Coefficients in Mixed Ionic Electronic Conducting Oxides from the Pressure Dependence of Oxygen Permeation. **1998**, *106*, 189–195.

(57) E. SIEBERT, A. H. and M. K. Impedance Spectroscopy Analysis of $La_{1-x}Sr_xMnO_3$-Yttria-Stabilized Zirconia Electrode Kinetics. *Electrochim. Acta* **1995**, *40*, 1741–1753.

(58) J. VAN HERLE, A. J. M. and K. R. T. A Study on the $La_{1-x}Sr_xMnO_3$ Oxygen Cathode. *Electrochim. Acto* **1996**, *41*, 1447–1454.

(59) Chen, X.J.; Khor, K.A.; Chan, S.H. Identification of O2 Reduction Processes at Yttria Stabilized Zirconia|doped Lanthanum Manganite Interface. *J. Power Sources* **2003**, *123*, 17–25.

(60) Jiang, S. P.; Love, J. G.; Ramprakash, Y. Electrode Behaviour at $(La,Sr)MnO_3/Y_2O_3–ZrO_2$ Interface by Electrochemical Impedance Spectroscopy. *J. Power Sources* **2002**, *110*, 201–208.

(61) Jiang, S. P. A Comparison of $O_2$ Reduction Reactions on Porous $(La,Sr)MnO_3$ and $(La,Sr)(Co,Fe)O_3$ Electrodes. *Solid State Ionics* **2002**, *146*, 1–22.

(62) Jiang, S. P. Development of Lanthanum Strontium Manganite Perovskite Cathode Materials of Solid Oxide Fuel Cells: A Review. *J. Mater. Sci.* **2008**, *43*, 6799–6833.

(63) Erica Perry Murray , Tsepin Tsai, S. A. B. Oxygen Transfer Processes in (La,Sr)$MnO_3$/$Y_2O_3$-Stabilized -Stabilized $ZrO_2$ Cathodes : An Impedance Spectroscopy Study. *Solid State Ionics* **1998**, *110*, 235–243.

(64) Zhu, H.; Kee, R. J.; Janardhanan, V. M.; Deutschmann, O.; Goodwin, D. G. Modeling Elementary Heterogeneous Chemistry and Electrochemistry in Solid-Oxide Fuel Cells. *J. Electrochem. Soc.* **2005**, *152*, A2427.

(65) S. B. Adler, J. A. L. and B. C. H. S. Electrode Kinetics of Porous Mixed-Conducting Oxygen Electrodes. *J. Electrochem. Soc.* **1996**, *143*, 3554–3564.

(66) Adler, S. B. Factors Governing Oxygen Reduction in Solid Oxide Fuel Cell Cathodes. *Chem. Rev.* **2004**, *104*, 4791–4843.

(67) Perry, M.; Newman, J.; Cairns, E. J. Mass Transport in Gas-Diffusion Electrodes : A Diagnostic Tool for Fuel-Cell Cathodes. *J. Electrochem. Soc* **1998**, *145*, 5–15.

(68) Horita, T.; Yamaji, K.; Sakai, N.; Yokokawa, H.; Kawada, T.; Kato, T. Oxygen Reduction Sites and Diffusion Paths at LaSrMnO Yttria-Stabilized Zirconia Interface for Different Cathodic Overvoltages by Secondary-Ion Mass Spectrometry. *Solid State Ionics* **2000**, *127*, 55–65.

(69) Brichzin, V.; Fleig, J.; Habermeier, H.; Maier, J. Geometry Dependence of Cathode Polarization in Solid Oxide Fuel Cells Investigated by Defined Sr-Doped LaMnO 3 Microelectrodes. *Electrochem. Solid-State Lett.* **2000**, *3*, 403–406.

(70) Brichzin, V.; Fleig, J.; Habermeier, H.; Cristiani, G.; Maier, J. The Geometry Dependence of the Polarization Resistance of Sr-Doped $LaMnO_3$ Microelectrodes on Yttria-Stabilized Zirconia. *Solid State Ionics* **2002**, *153*, 499–507.

(71) Fleig, J.; Baumann, F. S.; Brichzin, V.; Kim, H.-R.; Jamnik, J.; Cristiani, G.; Habermeier, H.-U.; Maier, J. Thin Film Microelectrodes in SOFC Electrode Research. *Fuel Cells* **2006**, *6*, 284–292.

(72) G. J. la O', B. Yildiz, a S. McEuen, and Y. S.-H. Probing Oxygen Reduction Reaction Kinetics of Sr-Doped $LaMnO_3$ Supported on $Y_2O_3$-Stabilized $ZrO_2$. *J. Electrochem. Soc.* **2007**, *154*, B427–B438.

(73) Lauret, H.; Hammou, a. Localization of Oxygen Cathodic Reduction Zone at Lanthanum Manganite/zirconia Interface. *J. Eur. Ceram. Soc.* **1996**, *16*, 447–451.

(74) F. H. van Heuveln, H. J. M. Bouwmeester, and F. P. F. van B. Electrode Properties of Sr-Doped $LaMnO_3$ on Yttria-Stabilized Zirconia, I. Three-Phase Boundary Area. *J. Electrochem. Soc.* **1997**, *144*, 126–133.

(75) Heuvein, F. H. van; and Bouwmeester, H. J. M. Electrode Properties of Sr-Doped $LaMnO_3$ on Yttria-Stabilized Zirconia, II. Electrode Kinetics. **1997**, *144*.

(76) Wang, S.; Jiang, Y.; Zhang, Y.; Yan, J.; Li, W. Promoting Effect of YSZ on the Electrochemical Performance of YSZ 1 LSM Composite Electrodes. *Solid State Ionics* **1998**, *113-115*, 291–303.

(77) Liu, M.; Wu, Z. Significance of Interfaces in Solid-State Cells with Porous Electrodes of Mixed Ionic–electronic Conductors. **1998**, *107*, 105–110.

(78) Mogens Mogensen, S. S. Kinetic and Geometric Aspects of Solid Oxide Fuel Cell Electrodes. *Solid State Ionics* **1996**, *86-88*, 1151–1160.

(79) Fleig, J. On the Width of the Electrochemically Active Region in Mixed Conducting Solid Oxide Fuel Cell Cathodes. *J. Power Sources* **2002**, *105*, 228–238.

(80) Akira Endo, Manabu Ihara, Hiroshi Komiyama, K. Y. Cathodic Reaction Mechanism for Dense Sr-Doped Lanthanum Manganite Electrodes. *Solid State Ionics* **1996**, *86-88*, 1191–1195.

(81) Gerischer, H. Wechselstrompolarisation von Elektroden Mit Einem Potentialbestimmenden Schritt Beim Gleichgewichtspotential I. *Z. Phys. Chem* **1951**, *198*, 216.

(82) M. Sluyters-Rehbach, J.H. Sluyters, in: A.J. Bard (Ed.), Electrochemical Chemistry, Vol. 4, Marcel Dekker, New York, **1970**, P. 68.

(83) M. Sluyters-Rehbach, J.H. Sluyters, in: E. Yeager, et Al. (Eds.), Comprehensive Treatise of Electrochemistry, Vol. 9, Plenum, New York, **1984**, P. 274.

(84) Bisquert, J. Theory of the Impedance of Electron Diffusion and Recombination in a Thin Layer. *J. Phys. Chem. B* **2002**, *106*, 325–333.

(85) Diard, J.-P.; Montella, C. Diffusion-Trapping Impedance under Restricted Linear Diffusion Conditions. *J. Electroanal. Chem.* **2003**, *557*, 19–36.

(86) Shin, E.-C.; Ahn, P.-A.; Seo, H.-H.; Jo, J.-M.; Kim, S.-D.; Woo, S.-K.; Yu, J. H.; Mizusaki, J.; Lee, J.-S. Polarization Mechanism of High Temperature Electrolysis in a Ni–YSZ/YSZ/LSM Solid Oxide Cell by Parametric Impedance Analysis. *Solid State Ionics* **2013**, *232*, 80–96.

(87) Gokhale, a. M.; Zhang, S.; Liu, M. A Stochastic Geometry Based Model for Total Triple Phase Boundary Length in Composite Cathodes for Solid Oxide Fuel Cells. *J. Power Sources* **2009**, *194*, 303–312.

(88) Zhang, S.; Gokhale, a. M. Computer Simulations of Topological Connectivity of the Triple Phase Boundaries in Solid Oxide Fuel Cell Composite Cathodes. *J. Power Sources* **2012**, *219*, 172–179.